A self-tuning approach toward maximal energy dissipation with application to active vibration isolation

van Hattum, Gerard

Award date:
2021

EINDHOVEN UNIVERSITY OF TECHNOLOGY
DEPARTMENT OF MECHANICAL ENGINERING
DYNAMICS AND CONTROL

MSC GRADUATION PROJECT

A self-tuning approach toward maximal energy dissipation with application to active vibration isolation

Author:
G.P.M. VAN HATTUM
Identity number S0731413

Supervisor:
Prof .Dr. H. NIJMEIJER
Prof .Dr.Ir. M.F. HEERTJES
Ir P.W.J.M NUIJ

DC2020.119
January 10, 2021

Preface

This thesis is the outcome of a master's project carried out within the Dynamics and Control group at the Mechanical Engineering department of the Eindhoven University of Technology in the Netherlands.

This thesis is performed with coaching from prof.dr. Marcel Heertjes, engineer and control competence leader at ASML and reseacher at TU/e.

I would like to thank Marcel for his supervising role, guidance and enthusiastic feedback during my project. When I was frustrated by practical issues, you motivated me and gave me confidence to go on. I also appreciate your efforts to review my chapters without causing any delay.
I was looking for a graduation project and my former colleague Pieter Nuij had a suggestion for a project, that required both theoretical as well as experimental skills. I would like to thank dr.Pieter Nuij, who supported me many times after working hours with the experimental setup. I would also like to thank prof.dr. Henk Nijmeijer for his personal attention to the project.

But above all I want to thank my wive and children for their support, encouragement, and understanding when I work during the evenings and in the weekend. These were tough years for both myself and my family, caused by physical as well as mental complaints.
The study started with the pre-master as a hobby in addition to a 40-hour job. After that, the master's degree and graduation was quite difficult in addition to a full-time job.

Gerard van Hattum, November 2020

Abstract

Many mechanical systems suffer from disturbances. These disturbances are generally undesirable because they influence the accuracy or performance of a process. To achieve attenuation of disturbances this thesis considers an active vibration isolation system. The goal of the thesis is to show that maximal energy dissipation can be obtained, within the vibration isolation structure, by appropriate tuning of its tuned-mass-damper parameters. Such a tuning is performed in an adaptive manner using an energy criterion that needs to be maximized on the spot with the vibration isolation system in the loop, and with disturbances exciting the system, the latter being generally unknown. In order to assess the energy dissipation in the damper of the system, the torque applied to the damper, and the velocity difference over the the damper is needed. Without using a torque sensor in the setup, this torque can be estimated indirectly by measuring the actuator current, i.e., use the actuator as a sensor. A gradient-based optimization towards maximum energy dissipation will be applied to the tuned-mass-damper (TMD) setup. The gradients will be obtained from the perturbation method, thus rendering the optimization approach fully data-based. Optimal stiffness and damping coefficients are found iteratively using the Gaus-Newton method. In the thesis, it will be shown that maximal energy dissipation renders optimal vibration isolation.

LIST OF SYMBOLS

Symbol	Unit	Description
$Ampl$	A/V	Transconductance amplifier
Amp	V/A	Sensitivity shunt resistor
D_g	m	Ground vibrations displacement
d_1	Nms/rad	Damping coefficient Payload system
d_2	Nms/rad	Dampings coefficient TMD system
D_1	Vs/rad	Damping PD controller Payload
D_2	Vs/rad	Damping PD controller TMD
H	-	Hessian
I_1	kgm^2	Inertia payload
I_2	kgm^2	Inertia Tune Mass Damper
I_p	A	Current motor Payload system
I_t	A	Current motor TMD system
J	Js	Objective function
k_1	Nm/rad	Stiffness Payload system
k_2	Nm/rad	stiffness Tune Mass Damper
K_e	Nm/A	Torque constant actuator
K_1	V/rad	Gain PD controller Payload
Kp	V/rad	Gain PD controller TMD
K_{rod}	Nm/rad	Torsion stiffness Tune Mass Damper
M_1	kg	Massa Payload system
M_2	kg	Massa Tune Mass Damper
N	-	Number of timestamps
PS	rad/V	Process sensitivity
Pd_2	Js	Energy dissipation damper TMD
r_1	m	Radius Payload system
r_2	m	Radius TMD system
T	Nm	Disturbance acting on payload system
T_r	-	Transmissibility function
U	V	Voltage
θ_1	rad	Rotation Payload
θ_2	rad	Rotation Tune Mass Damper
ω_r	rad/s	Resonance frequency
ω_a	rad/s	Anti-resonance frequency
ξ	%	Relative damping
γ	1/Js	Inverse input energy dissipation
∂	-	Gradient
γ_d	-	damped newton parameter for damping perturbations
γ_k	-	damped newton parameter for stiffness perturbations

CONTENTS

CHAPTER 1

INTRODUCTION

1.1 CONTEXT ACTIVE VIBRATION ISOLATION

Vibration platforms are used to isolate machines from ground vibrations and other disturbances. With the increasing precision of machines, the demands on vibration isolation have also increased [1]. The standard method to accomplisch vibration isolation is by mounting the Payload system on soft springs, which have a limited amount of a mechanical damping. Acting on this payload are the direct disturbances T and the indirect ground vibrations D_g. This is schematically depicted in Figure 1.1. As a result of the model structure in Figure 1.1, a low pass like filter characteristic is obtained with a cutoff frequency determined by $\omega_r = \sqrt{\frac{k_1}{M_1}}$, such that disturbances above the resonance frequency are naturally attenuated. Because the structural damping represented by damping coefficient d_1 is often very small, passive systems are complemented with control systems as to provide active damping to the system [2]. This however comes with a trade-off in the sense of isolation performance: while improving the damping properties, the passive isolation characteristics are often deteriorated. For this reason, we take a different approach in this thesis. Instead of improving the damping properties of the isolation system by control, an active tuned-mass-damper system is envisioned that depending on the disturbance level present more or less absorbs energy from the system and in that sense improves the vibration isolation performance of the system rather than enhancing its closed-loop isolation characteristics. The idea for an additional TMD in the above context at least dates back to measuring methods from the nineties, which were applied at Philips Centre for Manufacturing Technology. They used a measuring more specifically method that was able to discriminate noisy light ballasts from silent ones [3] [4] [5]. They measured the mechanical energy from the Device Under Test (DUT) by means of a mechanical damper onto which the DUT was mounted. The mechanical energy was measured with a so-called impedance head. Figure 1.2 depicts a schematic representation of the test setup. The impedance head measured the force and the acceleration of the vibration absorber at the same time. The energy dissipation in the mechanical absorber was subsequently estimated by the product of force and

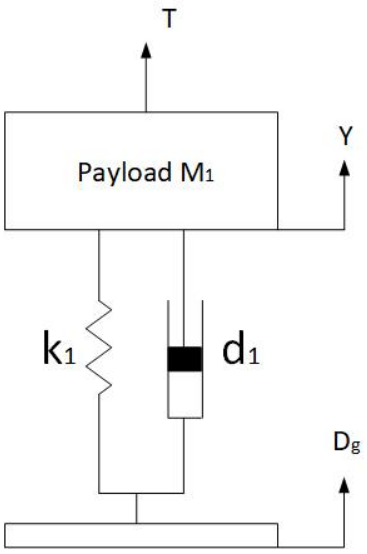

Figure 1.1: Model of a vibration isolation system

.

velocity. Differences in estimated energy dissipation formed an indication between silent and noisy light ballasts.

The idea for maximal energy dissipation forms the basis for this graduation project, and is investigated by applying a TMD at a payload system [6] [7]. Figure 1.3 depicts a schematic representation of a TMD system. Herein, m_1, m_2 represents the mass, respectively of the first and the second mass. k_1, k_2 represents the stiffness, respectively of the first mass to the fixed world and the stiffness between both masses, d_1, d_2 represents the damping coefficient, respectively of the first mass to the fixed world and the damping coefficient between both masses. T is the disturbance torque acting on the first mass and u_1 and u_2 are the displacements of mass 1 and 2, respectively. The limitations of a passive TMD have been recognized for example in [8] [9] [10], because only one disturbance frequency is attenuated, while by applying an active TMD and by tuning the stiffness k_2 and damping coefficient d_2 on the spot through some adaptive data-based control mechanism potentially provides the means to deal with arbitrary unknown frequencies [11]. So this thesis studies the principle of an active tuned-mass-damper system mounted on a vibration isolation structure that should be capable of dissipating energy from the vibration isolation structure by appropriate tuning of its tuned-mass-damper parameters. Ideally, such a tuning is done in an adaptive manner using an energy dissipation criterion that needs to be maximized automatically with the vibration isolation system in the loop.

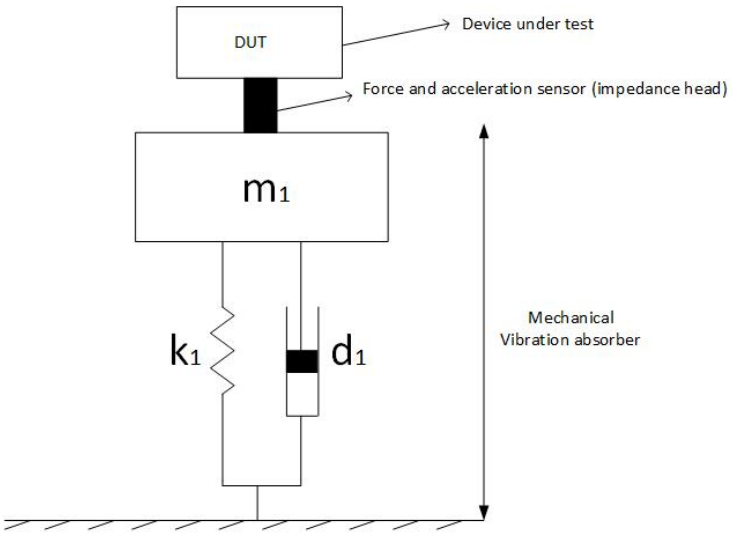

Figure 1.2: Setup to measure the light ballasts.

1.2 PROBLEM STATEMENT AND RESEARCH OBJECTIVES

In the active TMD from Figure 1.3 the spring k_2 and the damper d_2 will be mimicked by a PD controller in a feedback connection. The hypothesis that will be studied in this thesis is the following. Will maximum energy dissipation in the tuned-mass-damper system give rise to the best vibration isolation too? To verify this hypothesis a simulink model and an experimental setup have been designed and built. The following two research questions are posed.

Research Question 1:
To what extend do the stiffness and damping coefficients lead to maximal energy dissipation in the damper of the TMD and how does this provide the means for maximal attenuation of unknown disturbance frequencies?
Research Question 2:
How can the maximal energy dissipation be estimated in the absence of a direct force or torque sensor and how can such an estimation be effectively used in a data-driven optimization approach to modify the TMD parameters in an adaptive way depending on the (unknown) disturbance spectrum at hand?

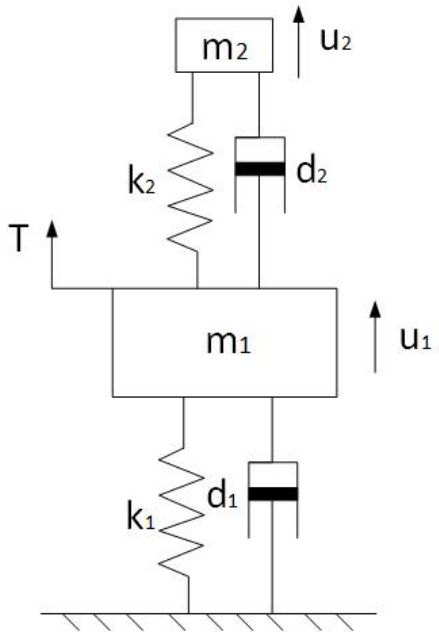

Figure 1.3: Model Tuned-Mass-Damper system.

1.3 Organization of the Thesis

This thesis is further organized as follows. Chapter 2 gives a description of the design and experimental modelling of an active vibration isolation system. The Payload system and the TMD system will be designed in a way that it allows for vibration isolation under active energy dissipation. Chapter 3 discusses the energy criterion to-be maximized. Given this criterion, firstly the occurrence of maximal energy dissipation will be studied for a passive system. Secondly, analytical and numerical results will be presented. In the last part of Chapter 3 it is explained how to estimate torque using measured actuator current. In Chapter 4, a gradient-based optimization scheme will be presented towards maximum energy dissipation. The gradients will be obtained from the perturbation method which is fully data-based. In Chapter 5 a proof of concept will be demonstrated on a real-life TMD system. Finally, in Chapter 6 conclusions are drawn and recommendations are given for further research.

CHAPTER 2

DESIGN AND EXPERIMENTAL MODELLING OF AN ACTIVE VIBRATION ISOLATION SYSTEM

In this chapter a description will be given of the design and experimental modelling of an active vibration isolation system. In Section 2.1 a description of the so-called PATO setup is given. PATO stands for 'Postacademisch Technisch Onderwijs'. The PATO setup will be used as a representative example for control, design, testing, and tuning. In Section 2.2, part of the PATO setup will be used to re-design the so-called 'payload' system. In Section 2.3, the remaining part of the PATO setup is re-designed into a TMD (tuned-mass-damper) system that allows for vibration isolation by active energy dissipation in the remainder of this report. This chapter is concluded with an outlook in Section 2.4.

2.1 PATO SETUP: PASSIVE FOURTH-ORDER SYSTEM

In this section a description will be given of the experimental fourth-order system further referred to as PATO setup. In the context of this graduation project, the PATO setup forms an excellent test system for self-tuning toward energy dissipation in vibration isolation systems as will be demonstrated at various locations throughout this report. It is simple of design but considered representative regarding its basic isolation principles for a large class of (industrial) vibration isolation systems.
This section is further organized as follows. In Subsection 2.1.1 the PATO setup will be introduced along with a description of its electronics, actuator, and encoder. In Subsection 2.1.2, the derivation of equations of motion of the PATO setup is given. In Subsection 2.1.3, a parametric identification will be done towards finding an estimate for the stiffness of the rod connecting the two rotating masses of the setup. In Subsection 2.1.4, a non-parametric identification will be performed and a comparison will be made with the derived fourth-order model.

2.1.1 INTRODUCTION PATO SETUP

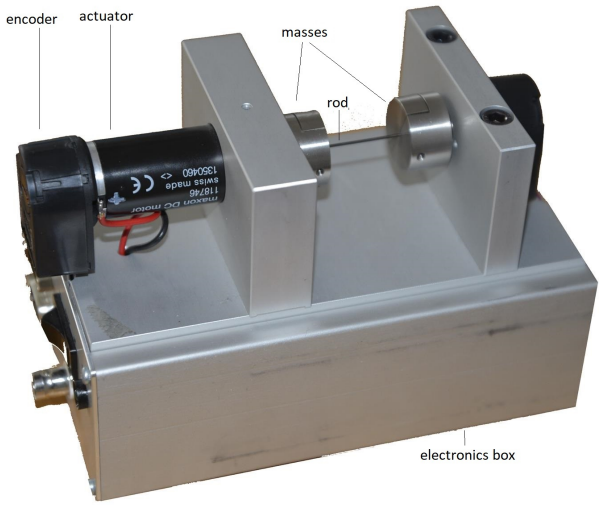

Figure 2.1: PATO system.

Figure 2.1 depicts the PATO setup. The actuator is a Maxon brushless DC motor [12]. The motor is driven by a voltage-to-current amplifier. The PATO system consist of two rotating masses, which are connected by a rod. Each mass is connected with a quadrature encoder. These are used to measure the angle of rotation in an incremental way with differential output (WEDS5541). The PATO setup is used in combination with an Ebox system, see Figure 2.2. The Ebox system is a 24 bits real time data acquisition system with two analog inputs and two analog outputs. Besides the ADC and DAC ports, the Ebox also contains encoder ports to count the pulse train from the quadrature encoder. The Ebox is connected via ethercat to a laptop to enable the use of matlab while operating under Ubuntu.

Figure 2.2: Ebox system.

2.1.2 FOURTH-ORDER MODEL

The PATO dynamics can be modeled by a simple parametric fourth-order system. Figure 2.3 depicts a schematic representation of such a fourth-order system. Herein, I_1, I_2 represent the mass inertia, respectively of the first and the second rotating mass, K_{rod} represents the rotation stiffness connecting both inertias, and d_2 represents the damping coefficient. T is the disturbance torque acting on the first inertia and θ_1 and θ_2 are the angle of rotation of inertia 1 and 2, respectively.

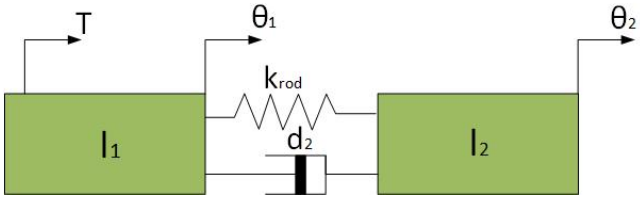

Figure 2.3: Fourth-order model representation.

In deriving the equations of motion for the fourth-order model, consider Newton's second law of motion, which for the load side gives:

$$M = I_1 \ddot{\theta}_1, \tag{2.1}$$

M is the total torque defined by:

$$M = T - M_v - M_d, \tag{2.2}$$

with M_v=$k_{rod}(\theta_1 - \theta_2)$ and $M_d = d_2(\dot{\theta}_1 - \dot{\theta}_2)$. Substitution of (2.2) in (2.1) gives:

$$I_1\ddot{\theta}_1 + d_2\dot{\theta}_1 + k_{rod}\theta_1 - k_{rod}\theta_2 - d_2\dot{\theta}_2 = T. \tag{2.3}$$

The equation of motion (2.3) can be transformed to frequency-domain giving

$$\begin{aligned} \theta_1(s)(I_1 s^2 + d_2 s + k_{rod}) - \theta_2(s)(d_2 s + k_{rod}) &= T(s) \\ \theta_1(s) &= \frac{(d_2 s + k_{rod})\theta_2(s) + T(s)}{I_1 s^2 + d_2 s + k_{rod}}. \end{aligned} \tag{2.4}$$

with s the Laplace variable.

For the measure side it holds that

$$\sum M = I_2\ddot{\theta}_2, \tag{2.5}$$

where M is the total torque defined by:

$$M = M_v + M_d, \tag{2.6}$$

and with M_v=$k_{rod}(\theta_1 - \theta_2)$ and $M_d = d_2(\dot{\theta}_1 - \dot{\theta}_2)$. Substitution of (2.6) in (2.5) gives:

$$I_2\ddot{\theta}_2 + d_2(\dot{\theta}_2 - \dot{\theta}_1) + k_{rod}(\theta_2 - \theta_1) = 0 \tag{2.7}$$

Similary, (2.7) can be transformed to frequency-domain giving:

$$\begin{aligned} \theta_2(s)(I_2 s^2 + d_2 s + k_{rod}) &= \theta_1(s)(d_2 s + k_{rod}) \\ \theta_2(s) &= \frac{d_2 s + k_{rod}}{I_2 s^2 + d_2 s + k_{rod}}\theta_1(s), \end{aligned} \tag{2.8}$$

Substitution of (2.8) in (2.4) gives:

$$\frac{\theta_1(s)}{T(s)} = \frac{I_2 s^2 + d_2 s + k_{rod}}{I_1 I_2 s^4 + d_2(I_1 + I_2)s^3 + (I_1 + I_2)k_{rod}s^2}. \tag{2.9}$$

The disturbance torque T applied at the motor side is generated by the actuator. The voltage (U) of the Ebox is transformed to a current, and the current (multiplied by the torque constant of the motor) gives T. The transconductance amplifier, that transforms U to current, is represented by the constant Ampl, while the torque constant of the actuator is represented by K_e, giving:

$$T \quad = \quad U * Ampl * K_e. \tag{2.10}$$

The transfer from U to θ_1 is thus given by:

$$\frac{\theta_1(s)}{U(s)} = Ampl * K_e * \frac{I_2 s^2 + d_2 s + k_{rod}}{I_1 I_2 s^4 + d_2(I_1 + I_2)s^3 + (I_1 + I_2)k_{rod} s^2} \tag{2.11}$$

substitution of (2.4) in (2.8) gives the transfer from U to θ_2.

$$\frac{\theta_2(s)}{T(s)} = \frac{d_2 s + K_{rod}}{I_1 I_2 s^4 + d_2(I_1 + I_2)s^3 + (I_1 + I_2)K_{rod} s^2}. \tag{2.12}$$

Substitution of (2.10) in (2.12) gives:

$$\frac{\theta_2(s)}{U(s)} = Ampl * K_e * \frac{d_2 s + K_{rod}}{I_1 I_2 s^4 + d_2(I_1 + I_2)s^3 + (I_1 + I_2)K_{rod} s^2}. \tag{2.13}$$

In order to assess the vibration isolation properties of the PATO setup and its corresponding fourth-order model, an often used measure is the so-called transmissibility function. Transmissibility is defined as the ratio between $\theta_2(s)$ and $\theta_1(s)$. The transmissibility function essentially is a transfer function that shows how much vibration is transmitted at a given frequency from θ_1 to θ_2. Therefore, the transmissibility function generally peaks at the natural frequency of the system. From (2.11) and (2.13), the transmissibility function is given by:

$$T_r(s) = \frac{\frac{\theta_2(s)}{U(s)}}{\frac{\theta_1(s)}{U(s)}} = \frac{d_2 s + k_{rod}}{I_2 s^2 + d_2 s + k_{rod}}. \tag{2.14}$$

2.1.3 PARAMETRIC IDENTIFICATION

In this subsection, a parametric identification will be conducted. As shown in the previous section, for vibration isolation performance the stiffness K_{rod} connecting the two masses plays a crucial role and as such needs to be identified in order to have an accurate parametric model. The torsion stiffness K_{rod} of the spring is determined by measuring the angle of rotation θ_1 and θ_2 and the torque T at the same time. The torque is generated by applying a force to inertia I_1. This force is measured with a force sensor. In the experiment, inertia I_2 is mounted to the fixed world so $\theta_2 = 0$. As a result, torque T equals the force multiplied by the radius. The test setup is depicted in Figure 2.4. Figure 2.5 depicts the results of the measurement of the torsion stiffness of the rod. The torsion stiffness is estimated at $\frac{0.1616}{0.6311} = 0.26\ \frac{Nm}{rad}$.

The values of both inertia's I_1 and I_2 are estimated too. First, the weight of both masses m_1 and m_2 (corresponding to I_1 and I_2, respectively) is determined, m_1=m_2=50 gram +/- 0.05 gram. The measured radii r_1 and r_2 (for inertias I_1 and I_2, respectively) are given by r_1=r_2 = 0.012 +/- $0.12e^{-3}$ meter.

The inertia's I_1 and I_2 are computed using : $I_1 = \frac{r_1^2}{m_1}$ and $I_2 = \frac{r_2^2}{m_2}$, giving $I_1 = I_2 = 3.6e^{-6} kgm^2$. In fact real-life the inertia I_1 and inertia I_2 are higher due to the inertia of the encoder and motor. The effective inertia I_1 is the sum of the inertia of I_1 (corresponding to m_1), encoder and motor. The inertia motor is estimated at

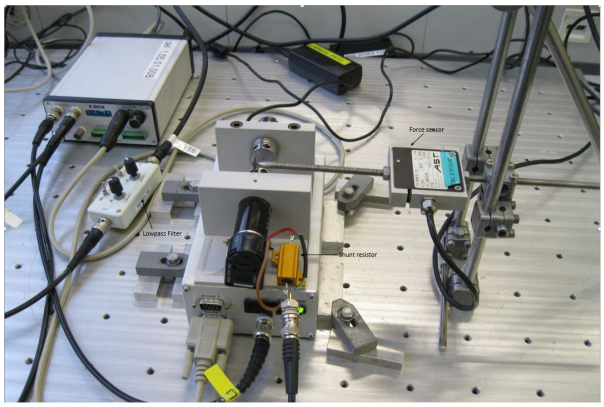

Figure 2.4: Setup for estimating the stiffness K_{rod}.

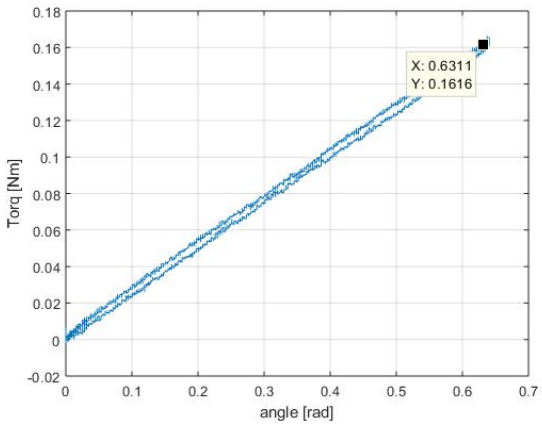

Figure 2.5: Measured angle-torque curves used for estimating K_{rod}

$1.06e^{-6}$ kgm^2 [12] and the inertia of the encoder is $0.05e^{-6}$ kgm^2. The effective inertia I_2 is the sum of the inertia of I_2 (corresponding to m_2) and the encoder. I_1 = $4.71e^{-6}$ kgm^2 and I_2 =$3.65e^{-6}$ kgm^2. In the next section these values are used for comparing the resulting parametric model with the result of a non-parametric identification.

2.1.4 NON PARAMETRIC IDENTIFICATION

For a torque input on the first mass and a sensor measurement at the same mass, hence the collocated control case, a non-parametric model, i.e., a frequency response function, is identified. The measurement result is obtained from closed-loop identification using the two-point method where measurement of the process sensitivity function as well as measurement of the sensitivity function together provide an estimate of the plant characteristics. The frequency response measurements are carried out with white noise as excitation signal. In the previous section a parametric identification has been conducted. In this section, both parametric and non-parametric models are compared.

Figure 2.6 depicts the measured frequency response function θ_1/U, which is compared with the parametric model. The frequency response is the ratio of the angle of rotation over the input voltage. The resonance (at 57.5 Hz) and anti-resonance frequencies (at 42.5 Hz) coincide. For frequencies beyond 150 Hz there is a poor signal-to-noise ratio. At 900 Hz an additional unmodeled resonance appears, which is likely due to the decoupling of the encoder. The sampling frequency used is 2048 Hz, which will give an additional phase delay of 90 degrees at 1024 Hz. The measured frequency response depicts more phase delay possibly due to the Ebox.

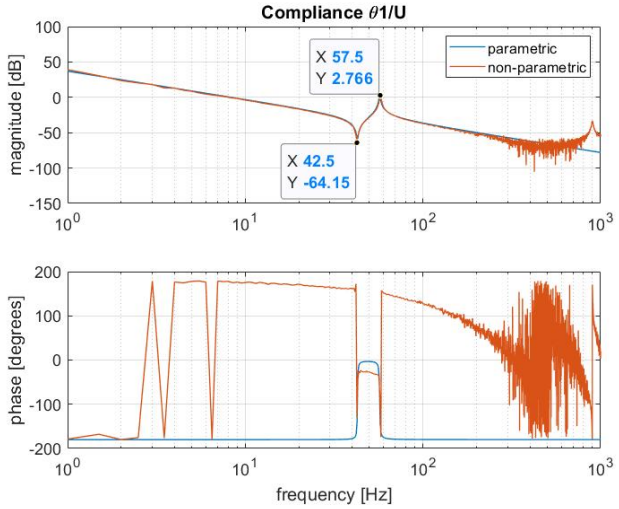

Figure 2.6: Measured frequency response function θ_1 over U.

Figure 2.7 depicts the measured frequency response function θ_2/U in comparison with the parametic model. Up to 150 Hz the parametric model matches well with the non-parametric model, but at higher frequencies sampling delay as well as a poor signal-to-noise ratio cause deviation between both models.

Figure 2.8 depicts the transmissibility from θ_1 to θ_2. The angle of rotation θ_2 highly exceeds the angle of rotation θ_1 at the resonance frequency. A peak occurs at

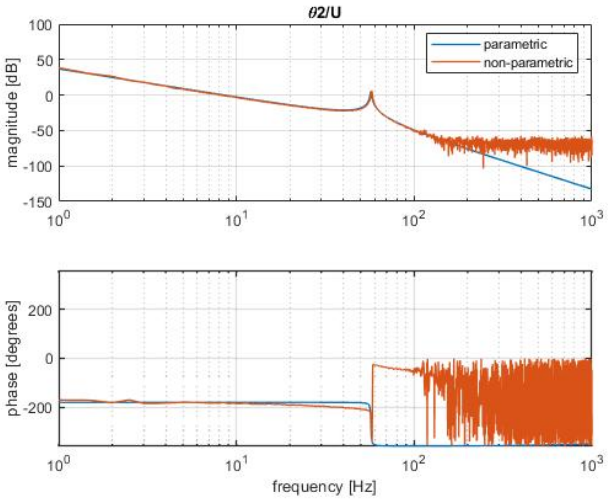

Figure 2.7: Measured frequency response function θ_2 over U.

the anti-resonance frequency shown in Figure 2.6.

In both Figures 2.6 and 2.7, the anti-resonance frequency can be calculated by:

$$\begin{aligned} \omega_a &= \sqrt{\frac{K_{rod}}{I_2}} \\ f_a &= \frac{1}{2\pi}\sqrt{\frac{0.26}{3.65e-6}} = 42,5 \text{ Hz}. \end{aligned} \tag{2.15}$$

The resonance frequency follows from:

$$\begin{aligned} \omega_r &= \sqrt{\frac{K_{rod}(I_1+I_2)}{I_1 I_2}} \\ f_r &= \frac{1}{2\pi}\sqrt{\frac{0.26(4.71e^{-6}+3.65e^{-6})}{4.71e^{-6} * 3.65e^{-6}}} = 56,6 \text{ Hz}. \end{aligned} \tag{2.16}$$

The calculated resonance frequency as well as the anti-resonance frequency corresponds well to the indicated frequency peaks in Figures 2.6 and 2.7, thus partly validating the parametric model from Subsection 2.1.2.

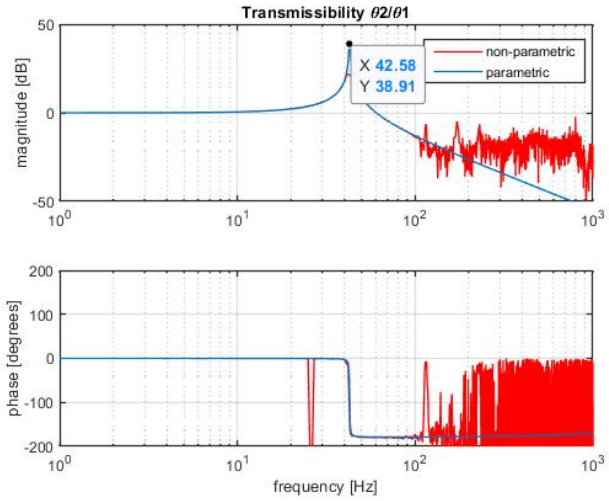

Figure 2.8: Measured frequency response function θ_2 *over* θ_1.

2.2 SECOND-ORDER PAYLOAD SYSTEM

The PATO setup discussed in Section 2.1 forms the basis for the design of the so-called payload system, i.e., a second-order vibration isolation system that will be actively controlled toward maximum energy dissipation in Chapters 3 and 4. In this section a description will be given on how the first mass is tuned at a selected frequency and damping. This supported mass is further referred to as the payload system. This section is further organized as follows. In Subsection 2.2.1 the payload will be introduced including a description of the actuator, sensor and mass inertia. In Subsection 2.2.2, a parametric identification will be conducted. In Subsection 2.2.3, a non-parametric identification of the payload system will be performed. In Subsection 2.2.4 the tuning of the feedback controller will be explained.

2.2.1 INTRODUCTION PAYLOAD SETUP

Figure 2.9 shows the payload setup. The rotating mass with inertia I_1 represents a cylinder made of stainless steel with m_1 = 99.2 +/- 0.05 gram and a radius r = 17 +/- 0.1 mm. The total inertia (as explained in the previous section) consists of the sum of the inertia mass, inertia motor and the inertia of the encoder. For the design of the payload setup a lightly damped system is preferred [13]. First, this matches with the large class of industrial vibration isolation systems based on airmounts. Second, the undamped resonance creates high sensitivity to disturbances which sets the appropriate conditions for the energy dissipation strategy in Section 3. As a basic setting of the payload system the following variables are chosen: resonance frequency of about 10 Hz and relative (dimensionless) damping ratio of approximately

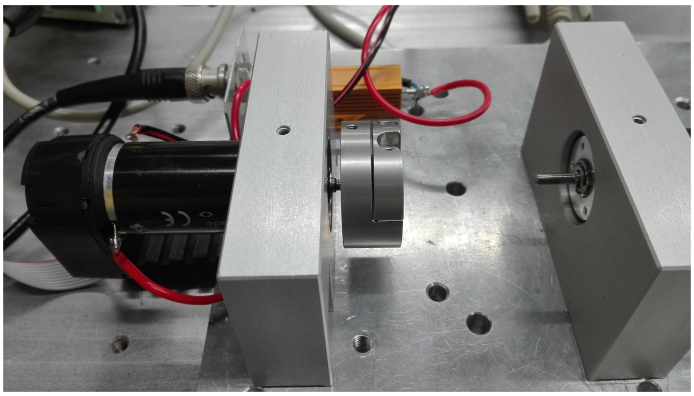

Figure 2.9: picture payload.

10 percent ($\xi = 0.1$). The spring and the damper are mimicked by applying a PD controller in a feedback control loop.

2.2.2 PARAMETRIC IDENTIFICATION

In this Subsection, a parametric identification of the second-order system will be conducted. The value of inertia I_1 is estimated using m_1 = 99.2 +/- 0.05 gram. The measured radius r_1 (for inertia I_1) is 17 +/- 01 mm. Part of the inertia I_1 is calculated using: $\frac{r_1^2}{m_1} = 14.3e^{-6}\ kgm^2$. The effective inertia I_1 is the sum of the inertia of I_1 (corresponding to m_1) encoder and actuator. The inertia of the motor is $1.06e^{-6}\ kgm^2$ [12] and the inertia of the encoder is $0.05e^{-6}\ kgm^2$ giving effectively $I_1 = 15.41e^{-6}\ kgm^2$. Figure 2.10 depicts a schematic model of the payload system. Herein, I_1 represents the mass inertia, k_1 represents the rotation stiffness and d_1 represents the damping coefficient. T is the disturbance torque acting on the mass and θ_1 is the angle of rotation.

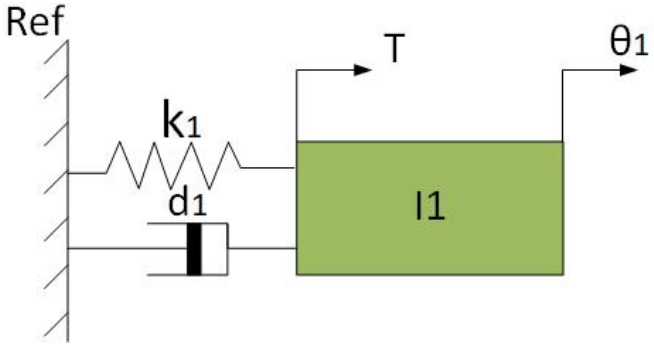

Figure 2.10: second-order model of the payload system.

The parameters d_1 and k_1 will be estimated from the measured process sensitivity function $\frac{\theta_1}{T}$ (compliance) using the known frequency as well as damping coefficient. In deriving the equations of motion for the payload system, consider Newton's second law of motion, which gives:

$$M = I_1\ddot{\theta}_1. \tag{2.17}$$

M is the total torque defined by:

$$M = T - M_v - M_d, \tag{2.18}$$

with M_v=$k_1\theta_1$ and $M_d = d_1\dot{\theta}_1$. Substitution of (2.18) in (2.17) gives:

$$I_1\ddot{\theta}_1 + d_1\dot{\theta}_1 + k_1\theta_1 = T. \tag{2.19}$$

The equation of motion in (2.19) can be transformed to frequency-domain giving

$$\begin{aligned} T(s) &= \theta_1(I_1 s^2 + d_1 s + k_1). \\ \frac{\Theta_1(s)}{T(s)} &= \frac{1}{I_1 s^2 + d_1 s + k_1}. \qquad (2.20) \\ \frac{\Theta_1(s)}{T(s)} &= \frac{\frac{1}{I_1}}{s^2 + \frac{d_1}{I_1} s + \frac{k_1}{I_1}}. \qquad (2.21) \end{aligned}$$

By evaluating (2.21) at s=$j\omega$ with $\omega = \omega_0$

$$\begin{aligned} &\frac{k_1}{I_1} = \omega_0^2 \ \ and \ \ \frac{d_1}{I_1} = 2\xi\omega_0 \qquad (2.22) \\ &k_1 = \omega_0^2 * I_1 = 0.057 \ \ Nm/rad \\ &d_1 = 2\xi I_1\omega_0 = \ \ 1.8 \ \ 10^{-4} \ \ \frac{Nm}{rad/s} \end{aligned}$$

2.2.3 NON PARAMETRIC IDENTIFICATION

Figure 2.11 shows the control schematics associated with Figure 2.10. Herein, U is the input voltage to the amplifier, I is the motor current and T is the mechanical torque acting on the mass. Block Ampl is the transconductance amplifier and K_e is the torque constant of the motor. Figure 2.11 shows that the plant (H) consists of the amplifier gain, the motor constant and the total mass inertia I_1.

Figure 2.12 shows at a frequency of 10 Hz an amplitude ratio of -8.6 dB, which corresponds with a factor of 0.37. With gain amplifier (ampl) = 0.5 $\frac{A}{V}$ and Torque constant(K_e) = 0.0439 $\frac{Nm}{A}$ [12]. Substitution of these values in (2.23) gives.

$$\begin{aligned} H &= \frac{ampl * K_e}{I_1 s^2} \\ I_1 &= \frac{ampl * K_e}{(2 * \pi * f)^2 * H} = 15e^{-6} \ \ \frac{kg}{m^2} \end{aligned} \tag{2.23}$$

The measured value and the estimated value are not exactly the same. This could be caused for example by the screw holes on the outside of the mass that are neglected in the mass estimation. The measured inertia is assumed to present the correct value.

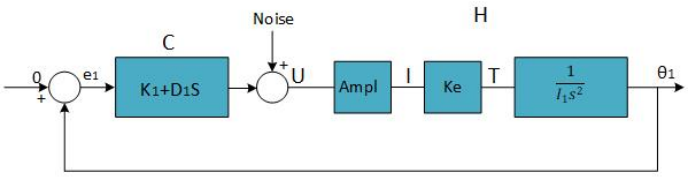

Figure 2.11: control scheme payload.

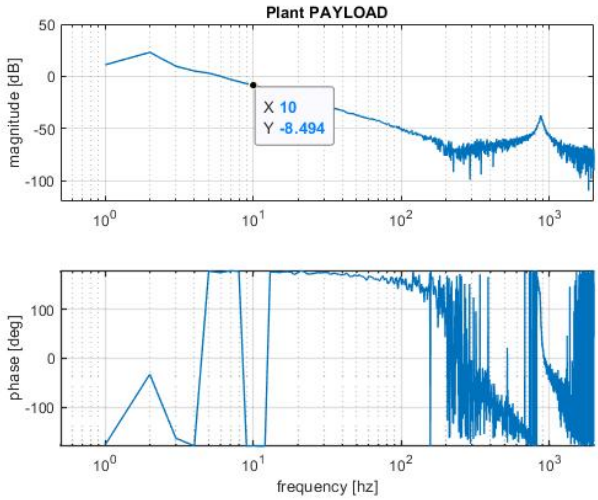

Figure 2.12: measured frequency response function of the plant H

2.2.4 CONTROLLER DESIGN

In this section the controller C will be discussed. In fact, the main motivation will be given as to why choosing a leadlag filter over a standard PD controller. The PD controller is given by

$$C(s) = K_1 + D_1 s. \tag{2.24}$$

$$K_1 = \frac{k_1}{ampl * K_e}. \tag{2.25}$$

$$D_1 = \frac{d_1}{ampl * K_e}. \tag{2.26}$$

Substitution of (2.25) and (2.26) in (2.24) gives

$$\begin{aligned} C(s) &= \frac{k_1}{ampl * K_e} + \frac{d_1}{ampl * K_e} s \\ &= 2.6 + 8,4e^{-3} s. \end{aligned} \tag{2.27}$$

Using f=10 in $s = j\omega_0$ = yields the complex number

$$C(j2\pi f_0) \quad = \quad 2,6 + 0,52\,j$$

The phase lead by the controller at 10 Hz is equal to

$$arctan\frac{0.52}{2.6} \quad = \quad 11,47 \ \ degrees$$

The breakpoint of a PD controller is given by:

$$\frac{K_1}{D_1} = 49,3 \ \ Hz$$

When the PD controller is applied, the closed-loop payload will start amplifying high-frequency noise. This is due to the fact that the gain of the controller is very large at high frequencies. The gain of the PD controller can be limited by adding a pole at higher frequencies, which results in a leadlag filter. Figure 2.13 shows the PD controller with a gain of 2,6 and a cutoff frequency of 49,3 Hz. The lead lag filter is calculated with the same phase lead and gain at 10 Hz but with limited gain at higher frequencies by using

$$C_{leadlag} = \left(\frac{\omega_p}{\omega_z}\right)\frac{s+\omega_z}{s+\omega_p} = \left(\frac{f_p}{f_z}\right)\frac{jf+f_z}{jf+f_p}. \tag{2.28}$$

Herein ω_p is the pole of the leadlag and ω_z its zero. f is chosen at $f = f_0 = 10$ Hz. The gain $\frac{f_p}{f_z}$ is omitted because it does not affect the phase behavior. f_z can be determined after placing the pole of the leadlag at 100 Hz. 100 Hz is chosen somewhat arbitrarily, giving.

$$C_{leadlag} = \frac{10j+f_z}{10j+100}. \tag{2.29}$$

The leadlag filter contains a pole at 100 Hz, a zero at 32 Hz and a gain of 2.6. Figure 2.13 depicts the leadlag filter and the PD controller by means of a Bode diagram. At 10 Hz both frequency response functions contain the same magnitude and phase lead. At high frequencies the gain of the lead lag filter falls (desirably) behind with respect to the gain of the PD controller.

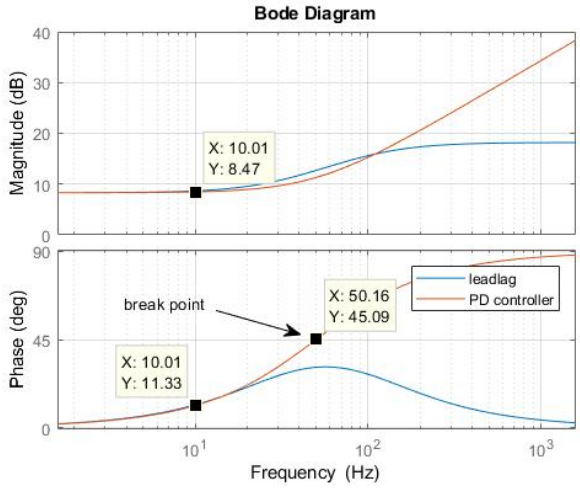

Figure 2.13: PD controller versus Leadlag filter.

In a closed-loop setting the parametric proces sensitivity estimate is compared with the proces sensitivity obtained from non-parametric identification. Notice that the non-parametric identification is obtained by a two point measurement. The parametric proces sensitivity function is already derived in (2.20).
but can be reformulated using

$$k_1 = K_1 * ampl * K_e. \tag{2.30}$$
$$d_1 = D_1 * ampl * K_e. \tag{2.31}$$

as

$$PS = \frac{ampl * K_e}{I_1 s^2 + d_1 s + k_1}. \tag{2.32}$$

The result of the identification is shown in Figure 2.14 by means of measured frequency response functions. Notice that a reasonable correspondence is obtained between both the parametric as well as the non-parametric identified models. At higher frequencies, sample delay as well as a poor signal-to-noise ratio causes deviation between both models. Also, higher-order dynamics (a zero around 250 Hz) become visible in the non-parametric model.

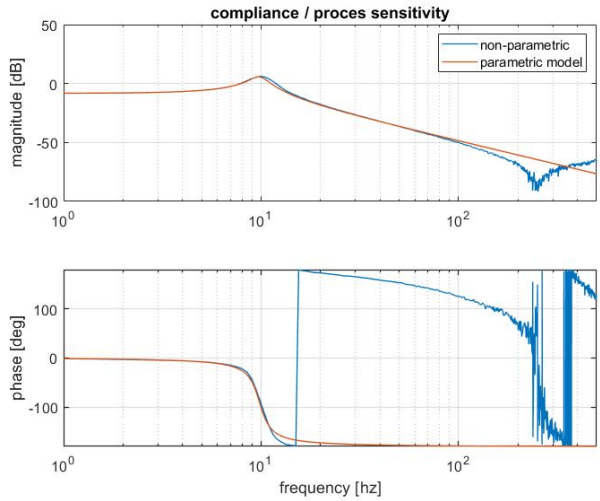

Figure 2.14: Measured frequency response functions of the process sensitivity.

2.3 ACTIVE TUNED-MASS-DAMPER CONFIGURATION

As the main research objective of this thesis is to design an active tuned-mass-damper system that maximizes energy dissipation of the payload system designed in Section 2.2, the remaining part of the PATO setup from Section 2.1 is redesigned to facilitate this tuned-mass-damper functionality. In this section a description will be given on how the second mass of the PATO setup is redesigned into an active tuned-mass-damper (TMD) system. This section is further organized as follows. In Subsection 2.3.1 the TMD will be introduced. In Subsection 2.3.2 a model will be presented. In Subsection 2.3.3 a parametric identification will be conducted, whereas in Subsection 2.3.4 a non-parametric identification will be performed.

2.3.1 DESIGN OF THE TMD SETUP

Figure 2.15 depicts the PATO setup but now in the context of an active tuned-mass-damper system. The active TMD is a specifically designed structural/mechanical element that can be incorporated into a new structure during the design phase or added to an existing structure to reduce the vibrations of that structure. TMD's are often effective if vibrations of the structure are related to one or more resonant modes, or if a disturbance occurs with its frequency content centered around a single harmonic frequency [10] [9] [14]. In Figure 2.15 I_2 is a cylinder made of aluminium which is much lighter than the used stainless steel of the payload system. Between the two inertia's a torsion spring is connected with torsion stiffness K_{rod} and damping d_2. The used actuator for I_2 is a Maxon brushless DC motor [12] which by means of control can alter the overall stiffness and damping properties experienced in the

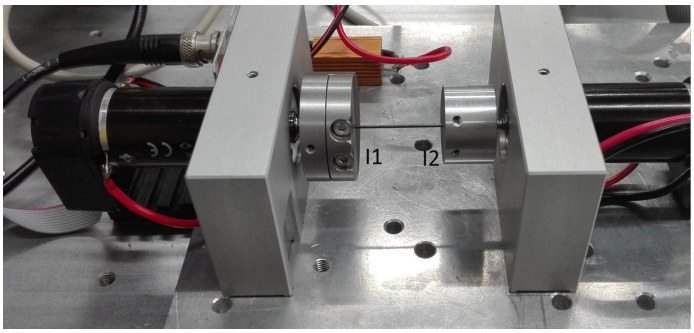

Figure 2.15: PATO setup viewed as a TMD system.

interconnection between I_1 and I_2. Hence the ability to provide active tuned-mass-damping.

2.3.2 FOURTH-ORDER MODEL OF THE TMD SYSTEM

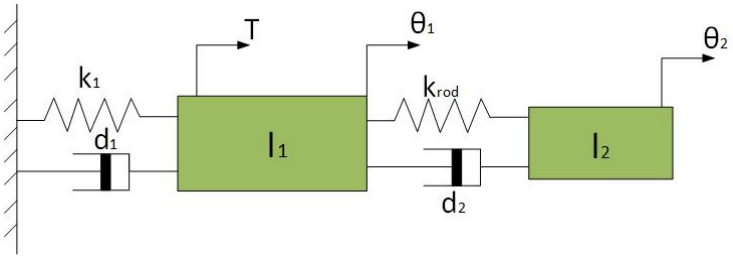

Figure 2.16: Fourth-order representation of the TMD system.

Figure 2.16 depicts a schematic representation of the TMD configuration. Herein, I_1, I_2 represents the mass inertia, respectively of the first and the second rotating mass, k_1, k_{rod} represents the rotation stiffness, respectively of the payload system to the fixed world and the rotation stiffness of the TMD, d_1, d_2 represents the damping respectively of the payload system and the damping of the TMD mass. T is the disturbance torque acting on the first mass and θ_1 and θ_2 are the angle of rotation of the payload and the angle of rotation of the tuned-mass-damper system. The stiffness k_1 and damping d_1 are already determined in Section 2.2.2. The initial rotation stiffness of the rod and damping d_2 are determined in Section 2.1.3. In deriving the equations of motion for the TMD model, consider Newton's second law, which for the payload side gives

$$M = I_1\ddot{\theta}_1, \tag{2.33}$$

with M the total torque defined by:

$$M = T - M_{v1} - M_{d1} - M_{v2} - M_{d2}, \tag{2.34}$$

and M_{v1}=$k_1\theta_1$, $M_{d1} = d_1\dot{\theta}_1$, M_{v2}=$K_{rod}(\theta_1 - \theta_2)$, $M_{d2} = d_2(\dot{\theta}_1 - \dot{\theta}_2)$. Substitution of (2.34) in (2.33) gives:

$$I_1\ddot{\theta}_1 + (d_1 + d_2)\dot{\theta}_1 + (k_1 + k_{rod})\theta_1 - k_{rod}\theta_2 - d_2\dot{\theta}_2 = T \tag{2.35}$$

The equation of motion in (2.35) can be transformed to frequency domain giving

$$\begin{aligned} \theta_1(s)(I_1 s^2 + (d_1 + d_2)s + (k_1 + k_{rod}) - \theta_2(s)(d_2 s + k_{rod}) &= T(s) \\ \theta_1(s) &= \frac{(d_2 s + k_{rod})\theta_2(s) + T(s)}{I_1 s^2 + (d_1 + d_2)s + (k_1 + k_{rod})}. \end{aligned} \tag{2.36}$$

Also, for the second mass it is found that

$$\sum M = I_2\ddot{\theta}_2, \tag{2.37}$$

where M is the total torque defined by:

$$M = M_{v2} + M_{d2}, \tag{2.38}$$

with M_{v2}=$K_{rod}(\theta_1 - \theta_2)$, $M_{d2} = d_2(\dot{\theta}_1 - \dot{\theta}_2)$. Substitution of (2.38) in (2.37) gives:

$$I_2\ddot{\theta}_2 + d_2(\dot{\theta}_2 - \dot{\theta}_1) + k_{rod}(\theta_2 - \theta_1) = 0 \tag{2.39}$$

In frequency-domain this gives

$$\theta_2(s) = \frac{d_2 s + k_{rod}}{I_2 s^2 + d_2 s + k_{rod}}\theta_1(s), \tag{2.40}$$

Substitution of (2.40) in (2.36) gives

$$\frac{\theta_1(s)}{T(s)} = \frac{I_2 s^2 + d_2 s + k_{rod}}{I_1 I_2 s^4 + \epsilon_1 s^3 + \epsilon_2 s^2 + \epsilon_3 s + \epsilon_4} \tag{2.41}$$

with $\epsilon_1 = I_1 d_2 + I_2(d_1 + d_2)$, $\epsilon_2 = I_1 k_{rod} + I_2(k_1 + k_{rod}) + d_1 d_2$, $\epsilon_3 = d_1 k_{rod} + d_2 k_1$, $\epsilon_4 = k_1 k_{rod}$.

In Section 2.1.2 it is found that the torque is equal to: T=U*Ampl*K_e. The transfer from U to θ_1 is thus given by:

$$\frac{\theta_1(s)}{U(s)} = Ampl * K_e * \frac{I_2 s^2 + d_2 s + k_{rod}}{I_1 I_2 s^4 + \epsilon_1 s^3 + \epsilon_2 s^2 + \epsilon_3 s + + \epsilon_4,} \tag{2.42}$$

which, after substitution (2.40) gives

$$\frac{\theta_2(s)}{T(s)} = \frac{d_2 s + k_{rod}}{I_1 I_2 s^4 + \epsilon_1 s^3 + \epsilon_2 s^2 + \epsilon_3 s + k_1 k_{rod}} \tag{2.43}$$

$$\frac{\theta_2(s)}{U(s)} = Ampl * K_e * \frac{d_2 s + k_{rod}}{I_1 I_2 s^4 + \epsilon_1 s^3 + \epsilon_2 s^2 + \epsilon_3 s + k_1 k_{rod}} \tag{2.44}$$

2.3.3 PARAMETRIC IDENTIFICATION

In the designed TMD setup a deliberate choice is made for two different mass inertia's, where I_1 is about 6 times the mass inertia of I_2. The value of mass inertia I_1 is already determined in Section 2.2. This estimated value is $15e^{-6}\ kgm^2$. I_2 is a cylinder of aluminium with a mass $m_2 = 20 + / - 0.05$ gram and a radius $r_2 = 12 + / - 0.1$ mm. The inertia I_2 is calculated using: $\frac{r_2^2}{m_2}$, giving I_2=1.4 $e^{-6}\ kgm^2$. The effective inertia I_2 is the sum of the inertia of I_2 (corresponding to m_2), encoder and motor giving effectively $I_2 = 2.51e^{-6}\ kgm^2$.

2.3.4 NON PARAMETRIC IDENTIFICATION

For a torque input on the first mass and a sensor measurement at the same mass, a frequency response function is identified. The measurement result is estimated from closed-loop identification where a measurement of the process sensitivity function is obtained. The frequency response measurents are carried out with white noise as excitation signal. In the previous section a parametric identification $\frac{\theta_1}{U}$ and $\frac{\theta_2}{U}$ has been conducted.

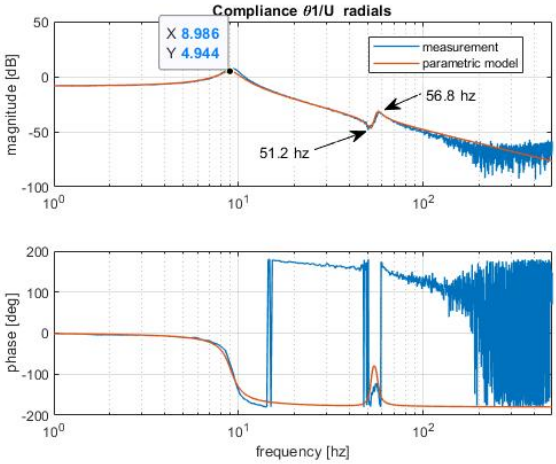

Figure 2.17: Compliances $\theta 1$ over U.

Figure 2.17 depicts the measured frequency response $\frac{\theta_1}{U}$ in comparison with the parametic model. The frequency response represents the ratio of the angle of rotation over the input voltage. The first resonance (at 8.98 Hz) coincides, but is somewhat lower than the original resonance of the payload system, which is due to the higher mass inertia(I_1 + I_2). The resonance at 56.8 Hz and the anti-resonance at 51.2 Hz coincide, whereby damping d_2 is tuned at $5e^{-5}\ \frac{Nms}{rad}$ so that the height of the resonance in the parametric model corresponds to the measurement results. For frequencies beyond 150 Hz there is a lot of uncertainty. The sample frequency used is 2048 Hz, which will give an additional phase delay that can be seen in the

non-parametric model, but which is not taken into account in the parametric model. The anti resonance frequency can be estimated with:

$$\omega_a = \sqrt{\frac{k_{rod}}{I_2}} \tag{2.45}$$

Where I_2 could be obtained from the measurement results as, $I_2 = \frac{k_{rod}}{\omega_a^2} = \frac{0{,}26}{(51{,}2*2*\pi)^2} = 2{,}51e^{-6}\ kgm^2$. The mass inertia ratio of I_2 and I_1 is 2,5:15 kgm^2. The resonance frequency can be calculated with the following formula:

$$f_r = \frac{1}{2\pi}\sqrt{\frac{k_{rod}(I_1+I_2)}{I_1 I_2}} = 56{,}4 \text{ Hz}. \tag{2.46}$$

Figure 2.18 shows the frequency response $\theta 2/U$ obtained from the measurement results compared with the parametric model. The resonance peaks coincides and the responses fairly match up until 150 Hz. Figure 2.19 shows the transmissibility

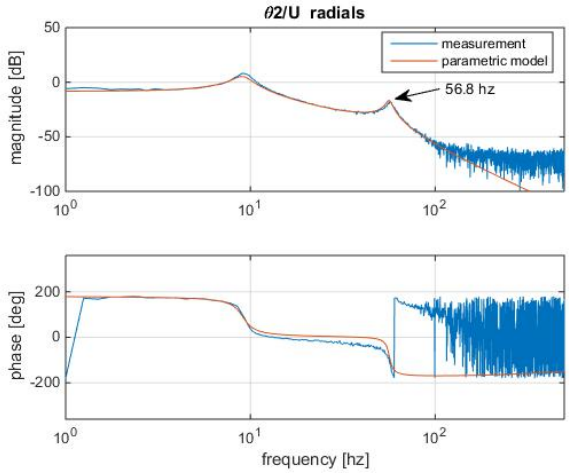

Figure 2.18: Frequency response $\theta 2$ over U.

function from θ_2 to θ_1. From the earlier parametric models, the transmissibility function is given by

$$\begin{aligned}\frac{\theta_2(s)}{\theta_1(s)} &= \frac{\frac{\theta_2}{U}}{\frac{\theta_1}{U}} \\ &= \frac{Ampl * K_e * \frac{d_2 s + k_{rod}}{I_1 I_2 s^4 + \epsilon_1 s^3 + \epsilon_2 s^2 + \epsilon_3 s + k_1 k_{rod}}}{Ampl * K_e * \frac{I_2 s^2 + d_2 s + k_{rod}}{I_1 I_2 s^4 + \epsilon_1 s^3 + \epsilon_2 s^2 + \epsilon_3 s + k_1 k_{rod}}} \\ &= \frac{d_2 s + k_{rod}}{I_2 s^2 + d_2 s + k_{rod}}\end{aligned} \tag{2.47}$$

Figure 2.19 shows that rotation of θ_2 mainly occurs at the anti-resonance frequency of 51,24 Hz as also shown in Figure 2.17. Beyond this frequency, mass I_2 rotates much less than mass θ_1. Below the resonance frequency, θ_1 equals θ_2.

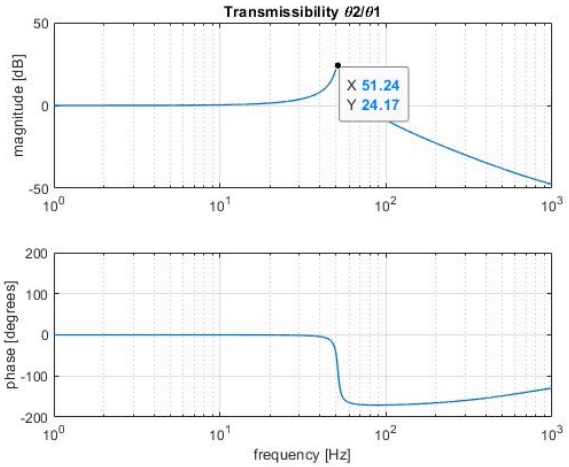

Figure 2.19: Transmissibility from $\theta 1$ to $\theta 2$.

2.4 SUMMARY

In this Chapter, the PATO setup has been discussed as a test environment for testing and demonstrating the objectives of this thesis. Both parametric as well as a non-parameteric models have been identified and compared. These models serve as a basis in the remaining chapters to further develop a method toward energy dissipation in vibration isolation systems.

CHAPTER 3

CONTROL TOWARD MAXIMUM ENERGY DISSIPATION

In this chapter, a control approach toward maximum energy dissipation will be proposed. The key idea is that an active tuned-mass-damper system mounted on a vibration isolation structure in principle should be capable of dissipating energy from the vibration isolation structure by appropriate tuning of its tuned-mass-damper parameters [15] [16]. Ideally, such a tuning is done in an adaptive manner using an energy criterion that needs to be maximized on the spot with the vibration isolation system in the loop. The latter is important because, though the dynamics of the vibration isolation system may be largely known, the disturbances exciting the system under operating conditions are generally unknown.

This chapter is further organized as follows. In Section 3.1 the energy criterion to-be-maximized will be discussed. Given this criterion, firstly the occurrence of maximal energy dissipation will be studied for a passive tuned-mass-damper system in Section 3.2. Secondly, the analytical results for a passive tuned-mass-damper system will be validated with numerical simulation results in Section 3.3. And thirdly, an active tuned-mass-damper system will be studied in Section 3.4. In Section 3.5 it is explained how to estimate torque using (measured) actuator current. The latter provides a crucial step in evaluating the energy criterion in the absence of a torque sensor, thus using only actuator current measurements. This chapter is concluded with an outlook in Section 3.6

3.1 DEFINITION ENERGY CRITERION

Consider a passive tuned-mass-damper (TMD) system with k_{rod} and d_2 its passive stiffness and damping coefficient, respectively. Figure 3.1 depicts a schematic representation of the model of the TMD system. With this model, simulations are carried out primarily to validate the hypothesis that minimal rotation θ_1 occurs at maximal energy dissipation in the damper with coefficient d_2 of the TMD system. Recall also from Chapter 2 that, k_1, k_{rod} represents the rotational stiffness, respectively of the

payload system to the fixed world and the rotational stiffness of the TMD, d_1, d_2 represent the damping respectively of the payload system and the damping of the TMD mass. T is the disturbance torque acting on the vibration isolation system with inertia I_1 and θ_1, θ_2 are the angle of rotation of the vibration isolation system and of the TMD respectively.

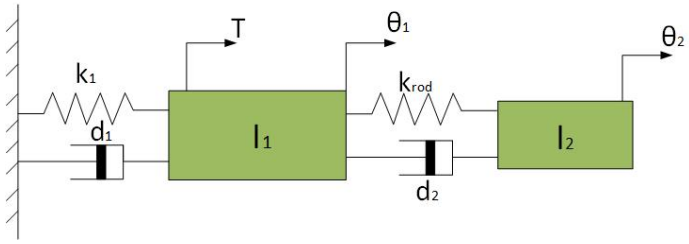

Figure 3.1: Fourth-order representation of the TMD system.

The energy dissipation in damper d_2, which will serve as the criterion for maximization, is given by:

$$P_{d_2} = d_2(\dot{\theta}_1 - \dot{\theta}_2)^2. \tag{3.1}$$

Note that (3.1) can be evaluated for example by using the estimated value for d_2 together with the velocities $\dot{\theta}_1$ and $\dot{\theta}_2$ resulting from encoder measurements.

3.2 Semi-analytical results of the passive TMD system

In this section the following parameters are obtained, the optimal stiffness K_{rod} and damping d_2 for maximum energy dissipation of the TMD system. The hypothesis is that these parameters lead to optimal vibration isolation performance of the payload system. The maximum energy dissipation is performed for disturbance frequencies of 5 Hz, 30 Hz and 70 Hz. Typically, 5 Hz is chosen below the resonance frequency of the payload system. 30 Hz is between the resonance of the payload system and the resonance of the TMD (51 Hz) and 70 Hz is chosen beyond the resonance of the TMD. These choices will be shown to support the generality of the hypothesis and hence the validity of the approach. The analytical results of the optimal stiffness and damping are validated with simulation results in Section 3.3.

Derivative of energy dissipation with respect to stiffness

Consider the objective function (dissipated energy):

$$J \ = P_{d_2}(\gamma) = d_2(\dot{\theta}_1 - \dot{\theta}_2)^2\gamma \tag{3.2}$$

with $\gamma = \gamma(K_{rod}, d_2)$ is the inverse input energy dissipation, which depends on K_{rod} and d_2, and which is used to normalize the dissipated energy in the damper with respect to the input energy, or

$$\gamma^{-1} = T\theta_1. \tag{3.3}$$

T is the (often unknown) disturbance torque acting on the vibration isolation system and θ_1 is the angle of rotation of the vibration isolation system. The velocity difference (e) is equal to $\dot{\theta}_1 - \dot{\theta}_2$ which is used to rewrite the objective function $J = d_2 e^T e\gamma$. The derivative of the objective function with respect to K_{rod} is given by:

$$\begin{aligned} \frac{\partial J}{\partial K_{rod}} &= d_2 \frac{\partial e^T}{\partial K_{rod}} e\gamma + d_2 e^T \frac{\partial e}{\partial K_{rod}} \gamma + d2e^T e \frac{\partial \gamma}{\partial K_{rod}}. \\ &= 2d_2 \frac{\partial e^T}{\partial K_{rod}} e\gamma + d_2 e^T e \frac{\partial \gamma}{\partial K_{rod}}. \end{aligned} \tag{3.4}$$

The gradients $\frac{\partial e}{\partial K_{rod}}$ and $\frac{\partial \gamma}{\partial K_{rod}}$ are estimated in simulink with the perturbation method (stepsize = $1e^{-7}$ Nm/rad) using the following first-order approximations:

$$\frac{\partial e}{\partial K_{rod}} \approx \frac{e(K_{rod} + \delta K_{rod}) - e(K_{rod})}{\delta K_{rod}}. \tag{3.5}$$

$$\frac{\partial \gamma}{\partial K_{rod}} \approx \frac{\gamma(K_{rod} + \delta K_{rod}) - \gamma(K_{rod})}{\delta K_{rod}}. \tag{3.6}$$

Simulations are done by varying K_{rod}. Maximal dissipated energy occurs if the derivative of the object function to K_{rod} in (3.4) equals zero. As can be seen in Figure 3.2 for a disturbance frequency of 5 Hz a clear maximum for the optimal value of K_{rod} is found at K_{rod} = 0,002367 Nm/rad where the energy dissipation is equal to 0.7468 W. For a disturbance frequency of 30 Hz, Figure 3.3 shows a clear optimal value of K_{rod} at 0,08487 Nm/rad where the energy dissipation is equal to 0.7899 W. In the lower plot of Figure 3.3 it is shown that the gradient $\frac{\partial J}{\partial K_{rod}}$ equals zero at the same stiffness value as found at the maximum energy dissipation, but there are also other zero crossings that associate with local maxima; for example at K_{rod} is 0.074 Nm/rad and K_{rod} is 0.076 Nm/rad . As can be seen in Figure 3.4 for the disturbance frequency of 70 Hz, a clear maximum is found at K_{rod} is 0,44 Nm/rad where the energy dissipation is equal to 0.73 W. As such, different disturbances require different values for K_{rod} to obtain maximum energy dissipation, hence the need for an adaptive mechanism.

From the analysis it is concluded that maximum dissipated energy occurs at $\frac{\partial J}{\partial K_{rod}} = 0$, but finding a value for K_{rod} where $\frac{\partial J}{\partial K_{rod}} = 0$ does not necessarily yield maximum energy dissipation. Stated differently the optimization problem is non-convex meaning that there is not necessarily a unique (global) optimum. Also, the optimal values for K_{rod} vary with varying disturbance frequency therefore hampering the effectiveness of a passive solution in which Krod is designed at a fixed value.

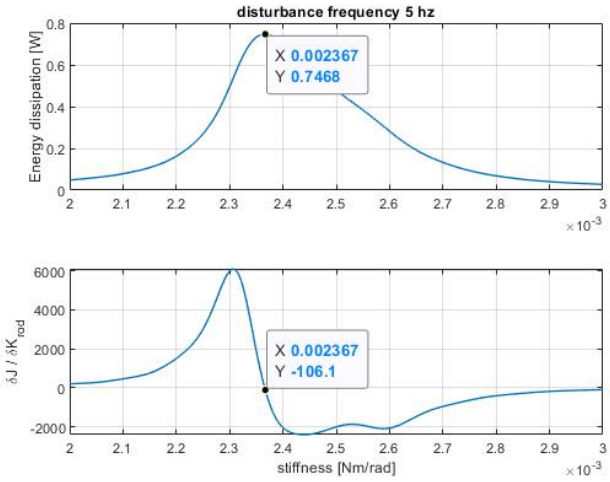

Figure 3.2: Derivative energy dissipation damper to K_{rod} for a 5 Hz disturbance.

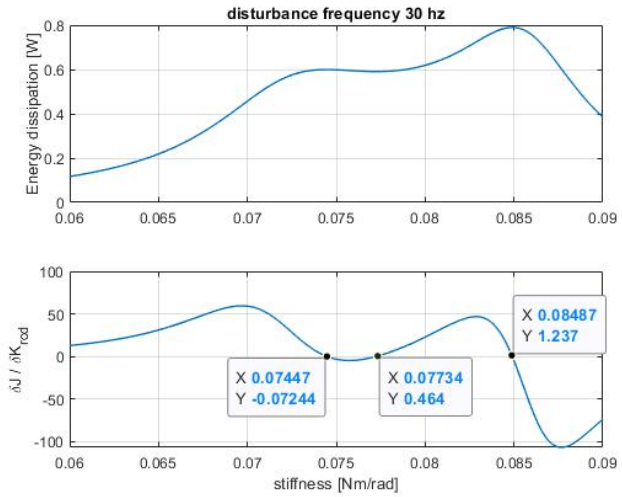

Figure 3.3: Derivative energy dissipation damper to K_{rod} for a 30 Hz disturbance.

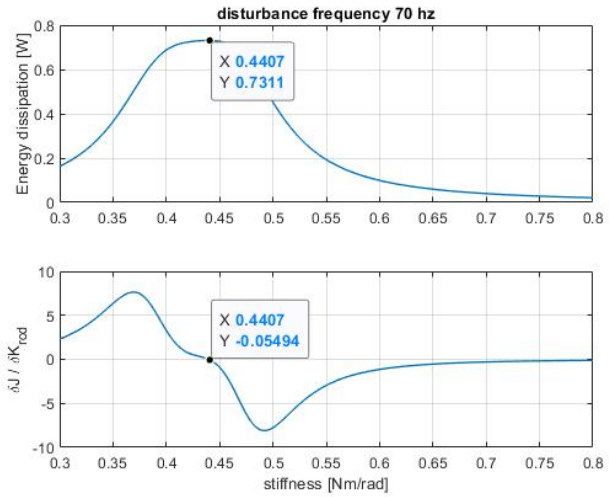

Figure 3.4: Derivative energy dissipation damper to K_{rod} for a 70 Hz disturbance.

3.2.1 DERIVATIVE OF ENERGY DISSIPATION WITH RESPECT TO DAMPING

The gradient of the objective function with respect to damper coefficient d_2 is given by:

$$\begin{aligned}\frac{\partial J}{\partial d_2} &= e^T e\gamma + d_2 \frac{\partial e^T}{\partial d_2} e\gamma + d_2 e^T \frac{\partial e}{\partial d_2}\gamma + d_2 e^T e \frac{\partial \gamma}{\partial d_2}. \\ &= e^T e\gamma + 2d_2 \frac{\partial e^T}{\partial d_2} e\gamma + d_2 e^T e \frac{\partial \gamma}{\partial d_2}. \end{aligned} \tag{3.7}$$

$\frac{\partial e}{\partial d_2}$ and $\frac{\partial \gamma}{\partial d_2}$ are estimated (stepsize = $1e^{-7}$ Nms/rad) in simulink with the perturbation method given the approximations (3.8) and (3.9) respectively.

$$\frac{\partial e}{\partial d_2} \approx \frac{e(d_2 + \partial d_2) - e(d_2)}{\partial d_2}. \tag{3.8}$$

$$\frac{\partial \gamma}{\partial d_2} \approx \frac{\gamma(d_2 + \partial d_2) - \gamma(d_2)}{\partial d_2}. \tag{3.9}$$

Numerical simulations are done by varying d_2, leading to the conclusion that maximal dissipated energy occurs if the derivative of the object function with respect to d_2 , or (3.7), equals zero. In the numerical simulations the stiffness coefficient values for K_{rod} are the same as determined in the previous section. As can be seen in Figure 3.5 for a disturbance frequency of 5 Hz a clear maximum is found at which the system dissipates energy. For the optimal value of $d_2 = 1.62e^{-6}$ Nms/rad the energy dissipation is equal to 0.75 W. In the lower plot of Figure 3.5 it is shown that $\frac{\partial J}{\partial d_2}$ indeed equals zero at this damping value thus potentially giving a good measure for finding the maximum amount of energy dissipation. For a disturbance frequency of 30 Hz, it can be seen in Figure 3.6 that the optimal value of $d_2 = 1.5e^{-5}$ Nms/rad where the energy dissipation is equal to 0.79 W. For a disturbance frequency of 70 Hz it can be seen in Figure 3.7 that also a clear maximum is found at which the system dissipates energy. Similar to the conclusion from the previous section, maximum dissipated energy can be found for those values where (3.7) becomes zero. Also note that increasing the disturbance frequency yields an increase in optimal damping values, that is , for frequencies [5, 30 70] Hz where values are found at [$1.62e^{-6}$, $1.5e^{-5}$, $7.19e^{-5}$] Nms/rad.

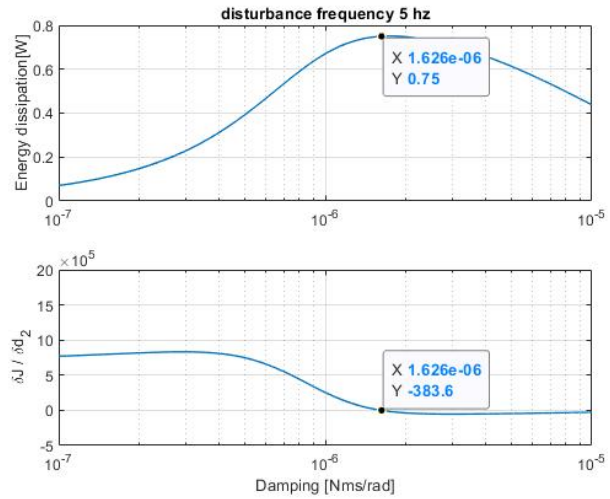

Figure 3.5: Energy dissipation as a function of damping coefficient d_2 under a 5 Hz disturbance."

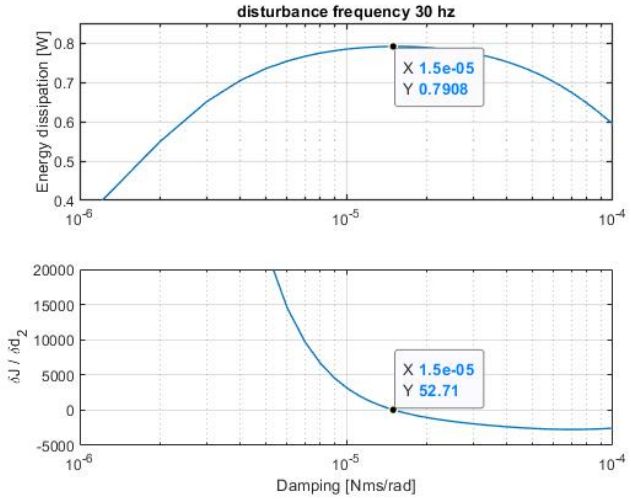

Figure 3.6: Energy dissipation as a function of damping coefficient d_2 under a 30 Hz disturbance.

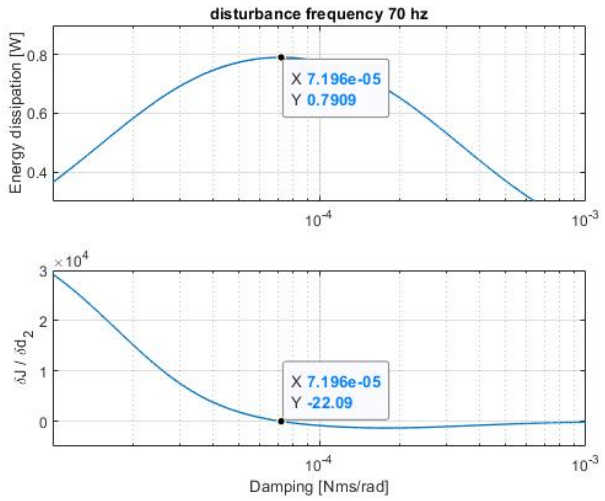

Figure 3.7: Energy dissipation as a function of damping coefficient d_2 under a 70 Hz disturbance.

3.3 Simulation results of the passive TMD system

In this section simulations results are discussed that couple maximum energy dissipation to optimal vibration isolation performance. Simulation results are obtained at the same disturbance frequencies as chosen in Section 3.2. Additionally, it will be examined if there exists a relation between the energy dissipation in d_2 and the rotation of the first mass θ_1, the latter being a measure for vibration isolation performance.

3.3.1 Grid of stiffness and damping values

In the simulations, the grid of both considered parameters K_{rod} and d_2 is chosen different for each disturbance frequency. For a disturbance frequency of 5 Hz the considered stiffness coefficients k_{rod} are logarithmically spaced in between $2e^{-3}$ to $3e^{-3}$ Nm/rad. Similarly, the grid of considered damping coefficients d_2 is varied from 10^{-7} to 10^{-4} Nms/rad.

3.3.2 Analysis over various frequencies

In this section, the result of various simulation studies will be discussed. The simulation context is given in Figure 3.8, which shows the used Simulink scheme. Input to the scheme is the disturbance signal T, that is chosen as a harmonic signal $T = sin(2\pi f(t))$ with f=5 Hz. Output to the scheme is the energy dissipation J according to (3.2). The simulation results refer to continuous-time simulations where

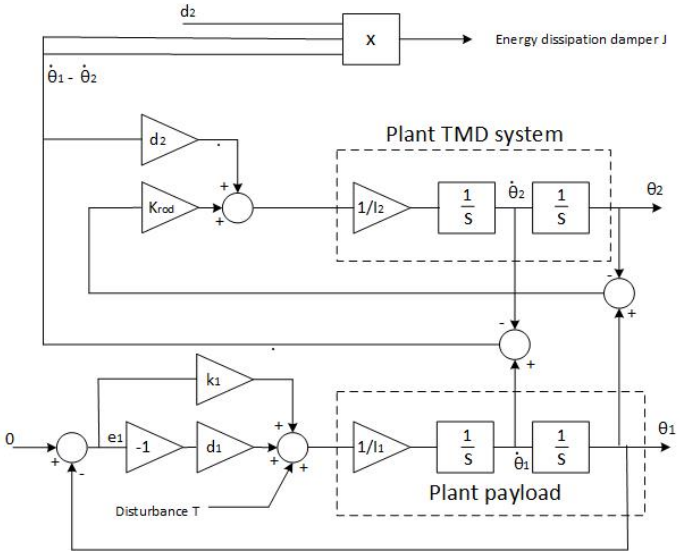

Figure 3.8: Applied simulink scheme for passive components.

the mean energy dissipation J in the damper is determined. Given the grid of stiffness and damping coefficients, Figure 3.9 shows that a clear maximum is found at which the system dissipates energy. That is, for the optimal values k_2 = 0.002385 Nm/rad and $d_2 = 2.134e^{-6}$ Nms/rad the energy dissipation equals $Jmax$ = 0.7087 W. Compared, for example, to the energy dissipation at the values $d_2 = 1e^{-6}$ Nms/rad and k_2 = 0.002 Nm/rad with J = 0.005 W the optimal values lead to a factor of 140 regarding improved dissipation, thereby indicating the relevance for an appropriate choice of the parameter values k_2 and d_2. The estimated stiffness and damping coefficients correspond with the values found earlier from with the semi-analytic calculations.

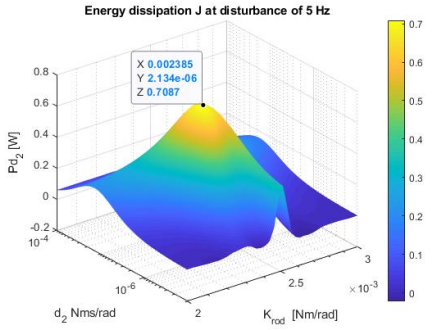

Figure 3.9: Maximal energy dissipation at disturbance of 5 Hz.

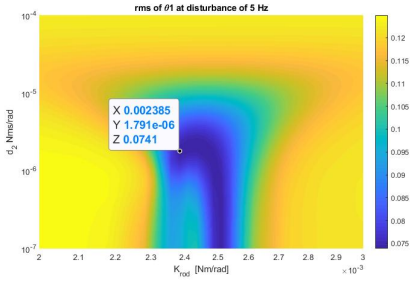

Figure 3.10: Rms of θ_1 at disturbance of 5 Hz.

Figure 3.10 depicts the influence of the disturbance at the payload system. In this 3D plot, the rotational stiffness K_{rod}, damping value d_2 and rms value of θ_1 are displayed. With an optimally tuned TMD, the rotation θ_1 has a minimum of 0.0741 radians, whereas with no TMD applied, the rotation of θ_1 is equal to 0,125 radial. The improvement in terms of vibration isolation properties of the payload system in terms of disturbance reduction is therefore 41%. This optimal value for the rotation of θ_1 occurs at the exact same optimal stiffness and damping values found for maximal energy dissipation, which has been shown in Figure 3.9. As such, it is concluded that in this case aiming for maximum energy dissipation translates well to the objective of optimal vibration isolation performance in view of a harmonic disturbance torque at 5 Hz. To validate the hypothesis that aiming for maximum energy dissipation of the TMD system leads to optimal vibration isolation performance of the payload system at arbitrary harmonic disturbance torques, two other frequencies will be checked: f_{dis} = 30 Hz and f_{dis} = 70 Hz. The stiffness of the rod is 0,26 Nm/rad, which will give an eigen frequency of the TMD with inertia I_2 of 52,4 Hz. In this case, the stiffness of the rod must decrease (add negative stiffness) to suppress the disturbance of 30 Hz [17]. Figure 3.11 depicts the optimal tuned TMD with k_{rod} equal to 0,0846 Nm/rad and d_2 becoming $1,3e{-}5$ Nms/rad. The estimated stiffness and damping coefficients corresponds with the values found with the semi-analytic computations from Section 3.2. For completeness Figure 3.12 shows the influence of the disturbance at the payload system at a disturbance frequency of 30 Hz. With an optimally tuned TMD, the rotation of θ_1 is 0,012 radial and if no TMD is applied, the rotation of θ_1 is equal to 0,021 radial. The disturbance reduction is 43%. The stiffness when energy dissipation is maximal corresponds with the stiffness leading to minimal rotation, but there is a slight difference in the damping constant. The results at a disturbance of 70 Hz are comparable to the previous cases and as such are shown in Appendix A

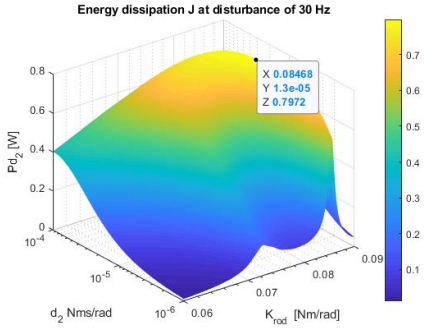

Figure 3.11: Maximal energy dissipation at disturbance of 30 Hz.

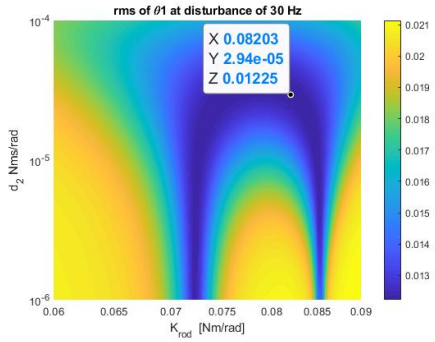

Figure 3.12: Rms of θ_1 at disturbance of 30 Hz

3.4 Simulation results with active TMD

Different from the previous analysis with passive elements, in this section a similar analysis is conducted but with active controller elements instead. Figure 3.13 depicts the control schematics associated with Figure 3.1. Herein, U is the input voltage to the amplifier of the payload system, respectively the amplifier of the TMD. I_p, I_t is the current to the motor of the payload system, respectively the TMD and T_p, T_t is the mechanical torque acting on the mass of the payload respectively the mass of the TMD. In Figure 3.13 it is shown that the rotational stiffness and damping constant between inertia I_1 and I_2 belong to an active and a passive part. The passive part (C passive) consists of the rotational stiffness of the rod k_{rod} and the damping constant d_2. The active part (C active) is represented by the PD controller parameters K_{p2} and D_2. Its parameter values can easily be changed (on-line) in software and thus can provide powerful knobs in online optimization of vibration isolation performance by maximizing the energy dissipation to unknown disturbances.

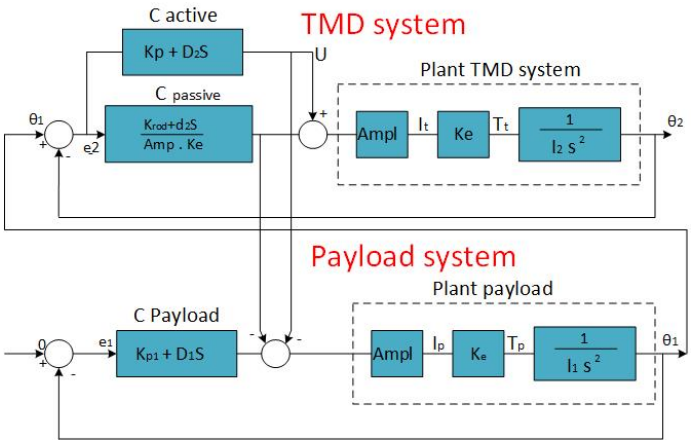

Figure 3.13: Control payload and adapted TMD system.

3.4.1 STIFFNESS AND DAMPING VARIATIONS

The rotational stiffness K_{p2} and the D action D_2 are varied while a harmonic disturbance is applied at inertia 1. The simulations are done for the same disturbance frequencies and the same reasons as already outlined in Section 3.3.2. Only the results tested at a disturbance frequency of 30 Hz are given, because the other (tested) frequencies give no additional information and correspond with the outcome of Section 3.3. The results tested at a disturbance frequency of 70 Hz are shown in Appendix B. At the same time, the mean and rms value of the output of the controller (U) are obtained and the rms value of the rotation of inertia I_1 is measured. The mean of the output of the controller is a ratio of the energy dissipated by the differential action of the controller. The output of the controller has a linear relation with the applied torque (see Section 3.5). Multiplying the torque with the angle velocity difference between inertia I_1 and inertia I_2 will give an estimate of the dissipated energy in the active damper D_2.

3.4.2 ANALYSIS OVER VARIOUS FREQUENCIES

In the 3D plots, the gain K_{p2} , D-action D_2 and energy dissipations Pd_2 are displayed. In Figure 3.14a, where the disturbance frequency is chosen between the resonance frequencies of the payload system and TMD (30 Hz) it is shown that the rms energy dissipation is maximal if the D action D_2 is at its boundary value of 10^{-6} and K_p is equal to -7.927. The effective stiffness between the two inertia's can be estimated from the passive and active part. The effective stiffness between the two inertias is equal to $K_{rod} + K_p * K_e * ampl = 0{,}086$ Nm/rad. In this case K_e represents the torque constant of the motor, and Ampl is the gain of the voltage to current amplifier. The calculated effective stiffness corresponds to an antiresonance frequency of 30.12 Hz which is calculated by Equation (3.10). This calculated effective stiffness corresponds

with an antiresonance frequency of 30.12 Hz estimated with Equation (3.10). Figure 3.14b shows approximately the same stiffness at the maximal dissipated energy but, the energy dissipation is much lower than the rms energy dissipation. The mean energy dissipation is maximal at a damping constant D_2 of 1.048 10^{-3} Vs/rad.

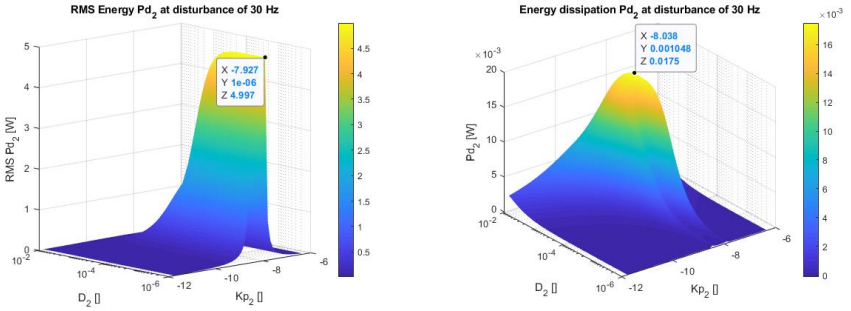

(a) (b)

Figure 3.14: (a) Rms dissipated energy of controller (b) mean dissipated energy of controller.

$$f_a = \frac{1}{2\pi}\sqrt{\frac{k^{eff}}{I_2}} \tag{3.10}$$

The effective damping between the two inertia's is given by:

$$\begin{aligned} D^{eff} &= D_2 * K_e * ampl \\ &= 2.3\ 10^{-5} Nms/rad \end{aligned} \tag{3.11}$$

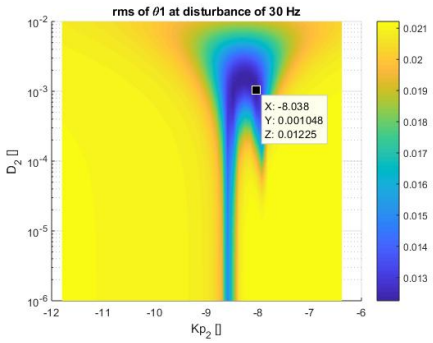

Figure 3.15: Rms rotation θ_1 at disturbance of 30 Hz

Figure 3.15 depicts the influence of the disturbance at the payload system. In this 3D plot, the gain of the controller Kp, D action D_2 and rms value of θ_1 are displayed.

With an optimally tuned PD controller, the rotation θ_1 has a minimum of 0.0125 radians and with no TMD applied, the rotation of θ_1 is equal to 0.021 radial. The improvement of vibration isolation properties of the payload system in terms of disturbance reduction is therefore 41%. This optimal value for the rotation of θ_1 occurs at the optimal PD controller values regarding maximal energy dissipation shown in Figure 3.11. As such, it is concluded that also in the active case aiming for maximum energy dissipation translates well to the objective of optimal vibration isolation performance in view of a harmonic disturbance torque at 30 Hz.

3.5 ACTUATOR USED AS SENSOR FOR ENERGY MEASUREMENT

In order to obtain the energy dissipation in damper d_2, the torque applied to the damper is needed. Without using a torque sensor, this torque can be estimated indirectly by measuring the current of the actuator. In this section a description will be given on how the actuator is used as sensor as well [18]. This will be done in preparation for the next chapter. The used actuator is a Maxon brushless DC actuator. The assumption is that in a DC actuator the current is a measure of the torque provided. Two methods are applied and compared to measure the mechanical torque. The first method is to measure the actuator current multiplied with the torque constant, which should correspond to the mechanical torque. The second method is to measure the force with a force sensor and to estimate the corresponding torque. In Section 3.5.1 a static torque measurement is performed and the results of both methods will be compared. In Section 3.5.2 a dynamic torque measurement will be performed.

3.5.1 STATIC TORQUE IDENTIFICATION

Figure 3.16 depicts the setup for measuring the static torque. The static torque is determined in two ways, by measuring the force with a force sensor and by measuring the current through the actuator. The torque is increased by ramping up the voltage to the input of the amplifier. The force sensor is placed at a certain distance (radius) from the centre of the mass. The mechanical torque is estimated by multiplying the force and radius. The current in the actuator is indirectly measured by measuring the voltage over a shunt resistance. The value of the shunt resistor is 0,1 Ω. The torque is estimated by multiplying the current in the maxon actuator with the torque constant. Figure 3.17 depicts the torque curves for both methods. Poor signal-to-noise ratio of the force sensor causes deviation between both methods.

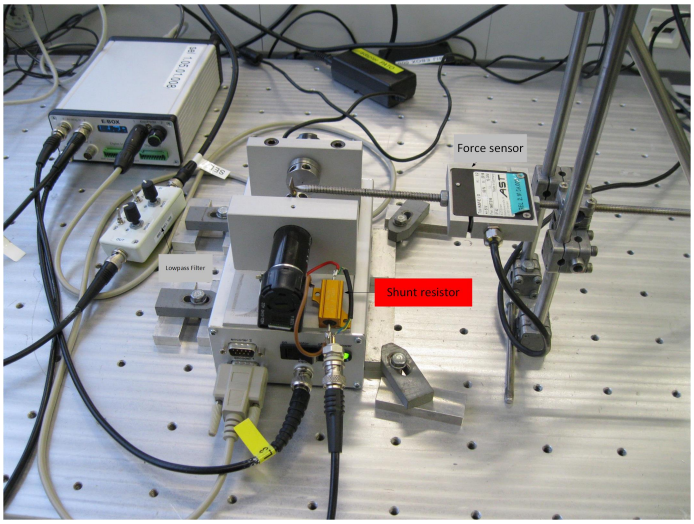

Figure 3.16: Setup for estimating the static torque.

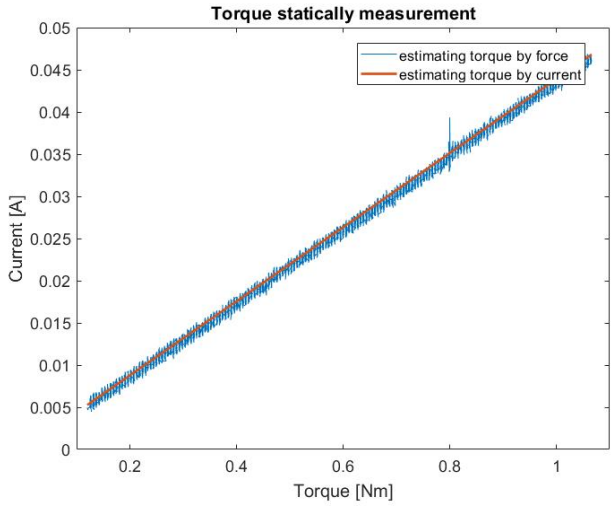

Figure 3.17: Estimated torque both with force sensor and by current in actuator.

3.5.2 DYNAMIC TORQUE IDENTIFICATION

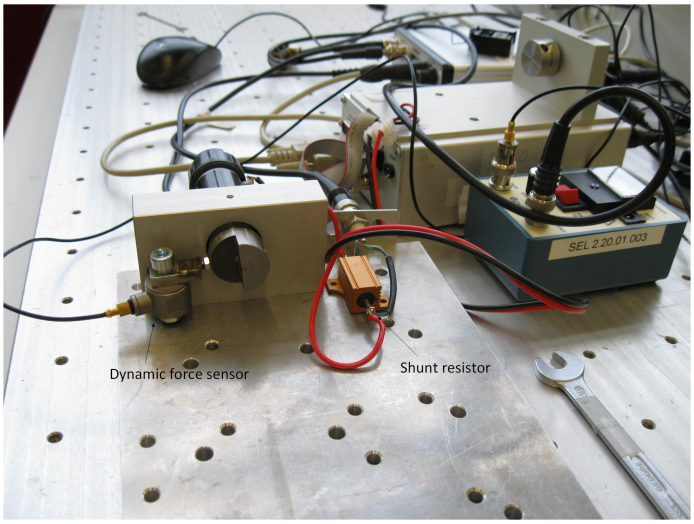

Figure 3.18: Setup to measure the torque dynamically.

Figure 3.18 depicts the setup for measuring the dynamical torque. The force sensor is mounted on the groundplate of the base in such a way that compared to the setup in the static measurements, the force sensor is more rigidly connected to the fixed world. For the excitation signal a zero mean white noise signal is used with a bandwidth of 500 Hz. The force is measured with a dynamic force sensor at a certain distance (radius) from the centre of the mass. The applied force transducer is an IEPE tensile and compressive sensor of Bruel&Kjaer, Type 8230 with a sensitivity of 44,52 N/V. The torque is calculated by multiplying the force and radius. The current is measured in the same way as the static measurements in Section 3.5.1. Figure 3.19 depicts the frequency response with noise excitation up to 500 Hz of the ratio of the torque of force sensor over the torque obtained by the current. The torque of the force sensor is obtained by multiplying the output of the force sensor with the radius and with the sensitivity of the force sensor. The torque determined with the current is obtained by multiplying the voltage over the shunt with the sensitivity of the shunt resistor and with the torque constant of the actuator. The required accuracy of the torque measurement is estimated to be within 5 per cent, this equates to 0.5 dB. Up to 150 Hz both torque measurement methods give equal results within a band of 0.5 dB. This leads to the conclusion that up to 150 Hz the torque can be estimated with the actuator current, which offers a simple solution. This is sufficient for the intended application. To investigate the higher harmonics the system is excited with white noise up to 1000 Hz. Figure 3.20 shows the frequency response with white noise excitation up to 1000 Hz. The measurement is less smooth due to the occurrence of higher harmonics. The amplitude ratio behaviour below 1Hz is caused by the AC

coupling of the force sensor. The frequency range of the force sensor is 1 Hz to 50 KHz. The measurement with the force sensor is limited by the first resonance frequency at 500 Hz. This resonance is caused by the bearing rigidity of the Maxon actuator.

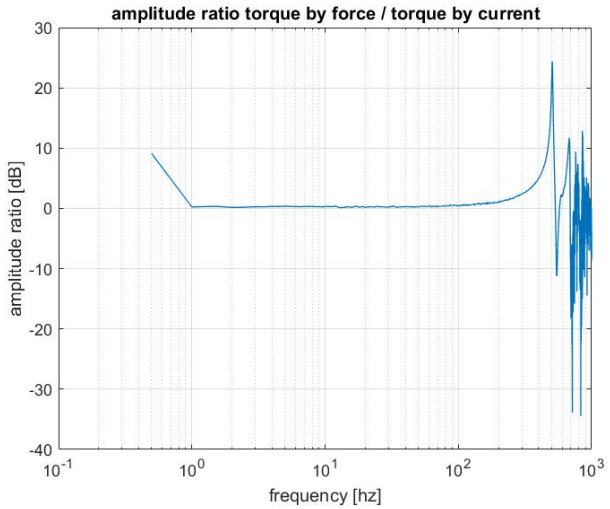

Figure 3.19: Dynamic torque measurement with white noise excitation up to 500 Hz.

The occurrence of the resonance frequencies around 900 Hz have been investigated with additional measurements. These measurements were carried out in open loop. Figure 3.21a shows the frequency response from the voltage over the shunt divided by the input voltage to the amplifier. Up to 1000 Hz the current is following the input voltage. The voltage-current amplifier is not the limiting factor. Figure 3.21b shows the frequency response from the encoder output to the voltage over the shunt resistor. For frequencies beyond 100 Hz, a poor signal-to-noise ratio gives a noisy measurement result. The mass inertia is not able to follow the signal input beyond 100 Hz. At 900 Hz an additional resonance appears, which is due to the decoupling of the encoder.

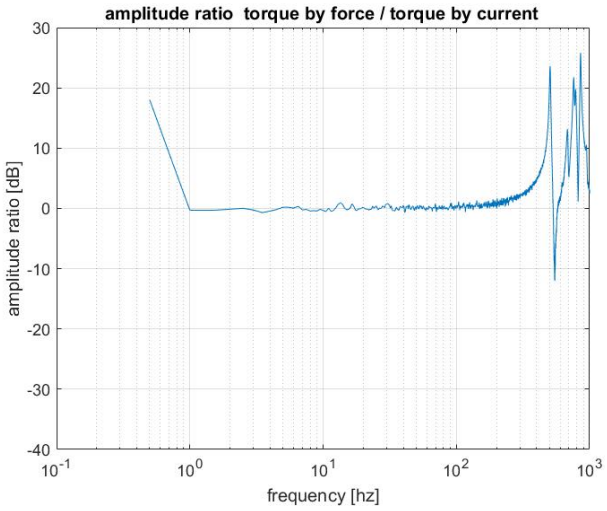

Figure 3.20: Dynamic torque measurement with white noise excitation up to 1000 Hz.

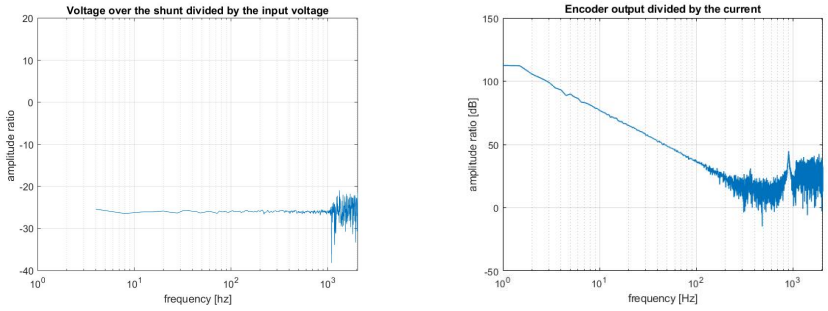

(a) (b)

Figure 3.21: (a) Measured FRF amplifier (b) measured FRF encoder.

3.6 SUMMARY

In this chapter the results lead to the following conclusions:
1. Maximal energy dissipation renders optimal vibration isolation, not only at a single frequency but at arbitrary harmonic disturbance frequencies.
2. Maximal energy dissipation is found at gradient values of the relevant parameters being equal to zero, hence the possibility to do (online) parameter optimization
3. In online parameter optimization, the energy criterion J does not need an explicit torque measurement but can be estimated through measuring the actuator current, i.e., use the actuator as a sensor.

CHAPTER 4

GRADIENT-BASED OPTIMIZATION APPROACH

In this chapter, a gradient-based optimization towards maximum energy dissipation will be applied to the tuned-mass-damper (TMD) setup. The gradients will be obtained from the perturbation method thus rendering the optimization approach fully data-based [19] [20] [21]. The key idea is that optimal values for the stiffness K_{rod} and damping coefficient d_2 are found with the machine in the loop while using the maximum energy criterion of Chapter 3. The spring and the damper are mimicked by applying a PD controller in a feedback control configuration. The stiffness K_{rod} is mimicked by K_p and the damper d_2 by D_2. This section is further organized as follows. In Section 4.1 energy optimization with perturbations on the stiffness values K_p and D_2 will be discussed. Secondly, the iterative procedure to keep updating K_p and D_2 is explained in Section 4.2. In Section 4.3, simulations results will be discussed and (to some extent) will be compared with the early simulations results obtained in Chapter 3. This chapter is concluded with an outlook in Section 4.4.

4.1 FINDING GRADIENTS THROUGH PERTURBATIONS WITH K_p

In a gradient-based optimization, gradients obtained from models, such as presented in Chapter 3, generally require sufficient model knowledge and as such are sensitive to model error. In a fully data-based manner, gradients can also be derived from data, for example by using the perturbation method [22]. In this method, as part discussed in Chapter 3, the perturbation is conducted on the active control elements thereby obtaining data under operating conditions, hence avoiding the risk of using too simple models. Essentially, the data are assumed to capture all relevant information for the optimization procedure. In terms of data-based control and optimization we

aim to find the optimal K_p that maximizes the cost criterion:

$$J_{(K_p)} = \frac{1}{N} d_2 e_{(K_p)}^T e_{(K_p)} \frac{1}{\gamma_{(K_p)}}. \tag{4.1}$$

with $e_{(K_p)} = \dot{\theta}_1(K_p) - \dot{\theta}_2(K_p)$, N >0 the number of timestamps, and $\gamma_{(K_p)}$ is the input energy. J_k corresponds with the energy dissipation in damper d_2. Let K_p in $J_k(K_p)$ be a set of controller parameters that maximizes the cost criterion J_k. With parameter vector K_p =[K_p^1 K_p^2...K_p^i...K_p^k] collect sampled-data $J_k(K_p)$. $\gamma(K_p)$ is used to normalize the dissipated energy in the damper with respect to the input energy.

Equation (4.1) gives rise to the following optimization problem:

$$\tilde{K}_p = \underset{K_p}{max} J_k. \tag{4.2}$$

Under certain conditions, the stiffness $\tilde{K}_p$ can be found iteratively using the Gaus-Newton method:

$$K_p^{i+1} = K_p^i - \gamma_k H_k^{-1} \partial J_k^T J_k. \tag{4.3}$$

With γ_k the damped newton parameter with a value of $0 < \gamma_k \leq 1$, and H_k denotes the Hessian matrix. The first-order approximation of the Hessian $H_k = H(K_p)$ is given by:

$$H_k \approx \partial J_k^T \partial J_k. \tag{4.4}$$

This approximation is often used for several reasons: (a) for many least squares problems the approximation is exact, (b) close to the optimum the approximation generally becomes very accurate, and (c) second-order derivatives are highly sensitive to noise present in the data and therefore are generally avoided.

In the update law (4.3), while using the approximate Hessian (4.4), the gradient $\frac{\partial J_k}{\partial k_p}$ can be found by the perturbation method via

$$\frac{\partial J_k}{\partial k_p} \approx \frac{J_k(K_p + \delta K_p) - J_k(K_p)}{\delta K_p}. \tag{4.5}$$

That is, by obtaining (for example from measurement) the sampled data $J_k(K_p + \delta K_p)$ while giving K_p a perturbed value δK_p and, subsequently, subtracting these data with the sample data $J_k(Kp)$. The gradient $\partial Jk/\partial K_p$ can be approximated in first order. From (4.5) it is clear that finding K_p in (4.2) with (4.3) requires both the data based gradients $\frac{\partial J_k}{\partial K_p}$ and the data J_k, which in this report are both fully based on data.

The optimal D_2 will be found similary by maximizing the cost criterion:

$$J_{(D_2)} = \frac{1}{N} d_2 e_{(D_2)}^T e_{(D_2)} \frac{1}{\gamma_{(D_2)}}. \tag{4.6}$$

$$\tilde{D}_2 = \underset{D_2}{max} J_d. \tag{4.7}$$

The stiffness D_2 can be solved iteratively using the Gaus-Newton method:

$$D_2^{i+1} = D_2^i - \gamma_d H_d^{-1} \partial J_d^T J_d. \tag{4.8}$$

With γ_d the damped Newton parameter for the damping perturbation with a value of $0 < \gamma_k \leq 1$, and H_d denotes the Hessian matrix. And an approximation of the Hessian $H_d = H(D_2)$ is given by:

$$H_d \approx \partial J_d^T \partial J_d. \tag{4.9}$$

$$\frac{\partial J_d}{\partial D_2} = \frac{J_d(D_2 + \delta D_2) - J_d(D_2)}{\delta D_2}. \tag{4.10}$$

4.2 Simulation scheme for determining gradients through perturbations

Figure 4.1 depicts the simulation schematics associated with the gradient estimation. Output to the scheme is the energy dissipation J according to (4.1) and (4.6). Results are obtained through continuous-time simulation where the energy dissipation J in the damper will be estimated continuously. The energy dissipation is estimated through the mean of the product of the output of the PD controller and the velocity difference of $\dot{\theta}_1 - \dot{\theta}_2$. Input to the scheme is the disturbance signal T, that is chosen

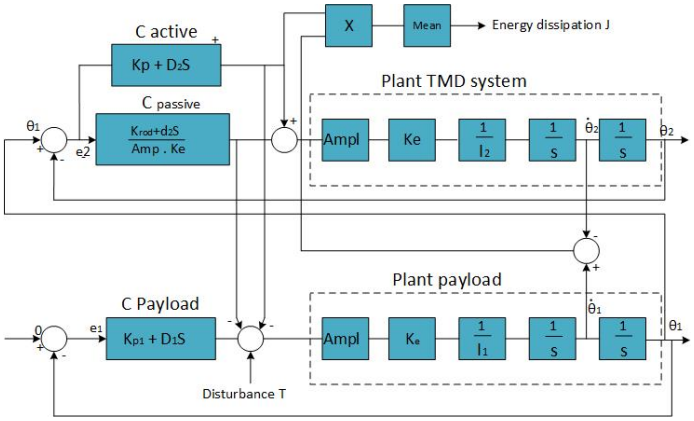

Figure 4.1: Simulation scheme used for online parameter optimization.

as a harmonic signal $T = sin(2\pi f(t))$ with the same frequencies as considered earlier in Section 3.2. The disturbance torque T is acting on the payload system. Figure 4.2 shows the sequence used to conduct the perturbations needed for the gradient estimation. The iteration is started with an initial value for the gain K_p and damping D_2. A reference simulation with the initial settings is carried out and the input energy and the dissipated energy (cost function) in D_2 are estimated. Subsequently K_p is

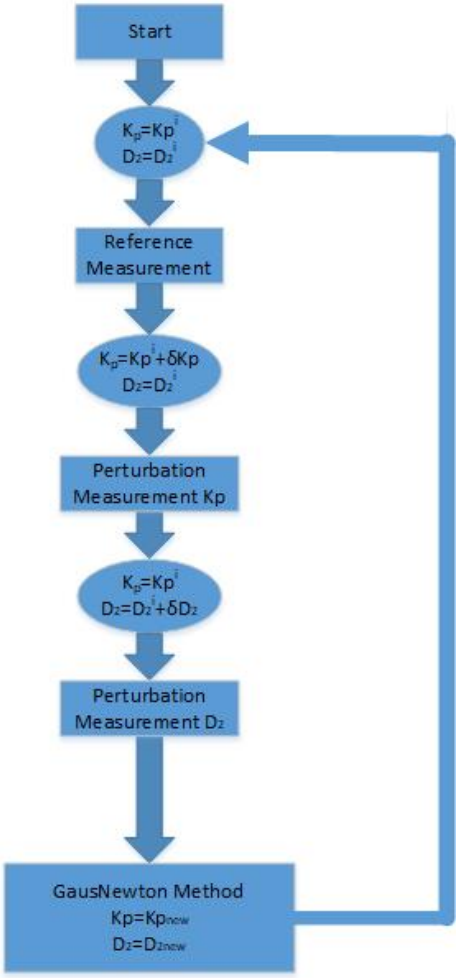

Figure 4.2: Sequence for the online parameter optimization.

perturbated with δK_p. The new dissipated energy is estimated, the gradient ∂J_k due to the proportional control action (K_p) and the Hessian H_k are estimated. With the Gaus-Newton method an updated K_p is given according to the update law in (4.3). The next step is to perturb D_2 with δD_2. The new dissipated energy is estimated with

the corresponding gradient ∂J_d and Hessian H_d. With the Gaus-Newton method a new D_2 is estimated according to the update law in (4.8). For the next iteration, the update K_p and D_2 are used in the simulation model. The chosen perturbation parameter is set at 1e-6 and 1e-7 for δK_p and δD_2, respectively. The chosen damped Newton parameter is set at 0.015 and 0.025 for γ_k and γ_d, respectively.

4.3 SIMULATIONS RESULTS

In this section numerical simulations results are presented for the Gauss-Newton optimization approach. These results are compared with the results of Section 3.2 and Section 3.3, which serve for validation purposes of the gradient-based optimization approach. As can be seen in Figure 4.3 for a disturbance frequency of 5 Hz the optimal K_p respectively the optimal D value is found at -11.73 V/s and $7.82e^{-5}$ Vs/rad after roughly 10 iterations. The effective stiffness is equal to $K_{rod} + K_p * K_e * ampl$=0.0025 N/rad and the real damping is $D_2 * K_e * ampl$= $1.72e^{-6}$ Nms/rad. Where K_e represents the torque constant of the motor, and Ampl is the gain of the voltage to current amplifier. The estimated stiffness and damping coefficient correspond to the values found with the semi analytical approach in Section 3.2. Figure 4.4 depicts the time data with and without applied TMD. With TMD the root mean square (RMS) of the Payload system is 0.074 radians and without TMD the influence of the disturbance at 5 Hz is 0.127 radians. The improvement in terms of vibration isolation properties of the Payload system in terms of disturbance reduction corresponds to the earlier found value of 41 %.

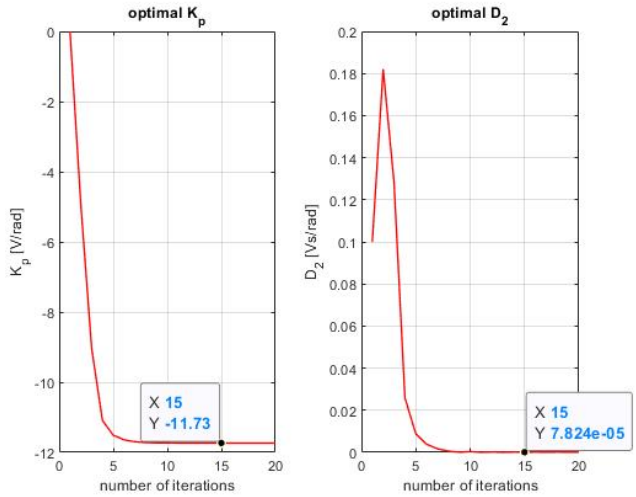

Figure 4.3: Perturbation of K_p and D_2 at a 5 Hz disturbance.

As can be seen in Figure 4.5 for a disturbance frequency of 30 Hz optimal K_p

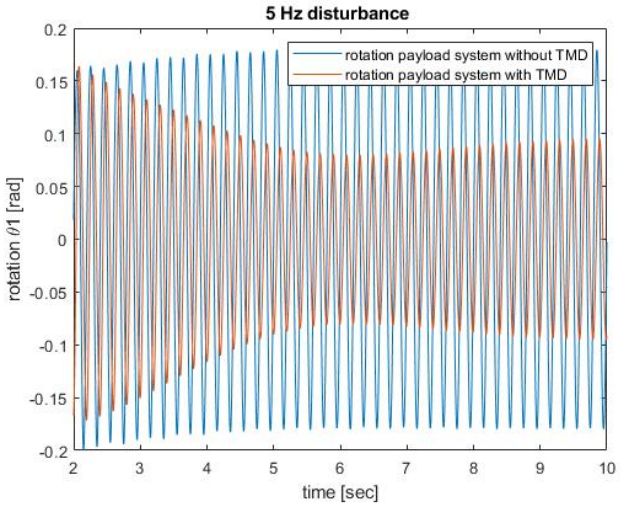

Figure 4.4: Response Payload system with and without TMD at a 5 Hz disturbance.

and D_2 values of the TMD controller are found at -8.013 V/rad and 0.001631 Vs/rad respectively. These values correspond with an effective stiffness of 0.0841 Nm/rad and damping coefficient of 3.58e-5 Nms/rad respectively. Figure 4.6 depicts the time data with and without applied TMD. With TMD the root mean square (RMS) of the Payload system is 0.0123 radial and without TMD the influence of the disturbance of 30 Hz is 0.021 radians. These values also corresponds well with the simulation results presented in Section 3.3. The improvement in terms of vibration isolation properties of the Payload system in terms of disturbance reduction is similarly 43 %. Figure 4.7 gives the optimal K_p (7.55 V/rad) and D action (0.003849 Vs/rad) of the TMD controller. By multiplying these values by the motor constant and the gain of the amplifier, the effective stiffness (0.426 Nm/rad) and damping (8.5e-5 Nms/rad) is obtained. The stiffness corresponds with the simulation results in Section 3.3 but there is a slight difference in the damping coefficient (14%). Figure 4.8 gives the time response with and without TMD. With applied TMD the root mean square (RMS) of the Payload system is 0.0055 radians and without TMD the influence of the disturbance frequency of 70 Hz is 0.0092 radians. These values corresponds with the simulation results in Section 3.3. The improvement in terms of vibration isolation properties of the Payload system in terms of disturbance reduction is similarly 42 %.

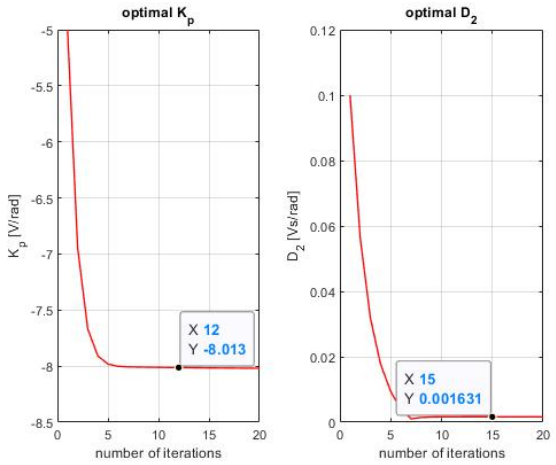

Figure 4.5: Perturbation to K_p and D at a 30 Hz disturbance.

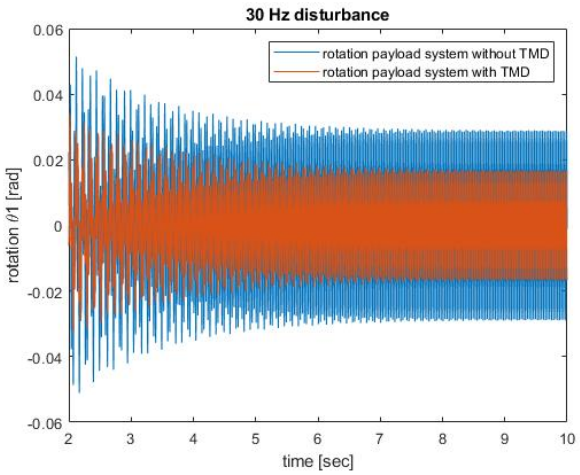

Figure 4.6: Response Payload system with and without TMD at a 30 Hz disturbance.

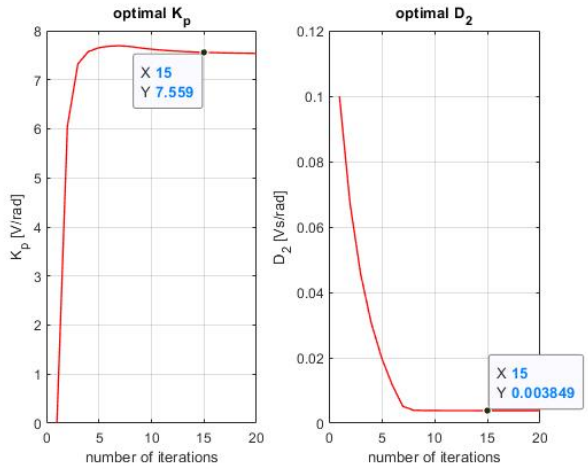

Figure 4.7: Perturbation to K_p and D at a 70 Hz disturbance.

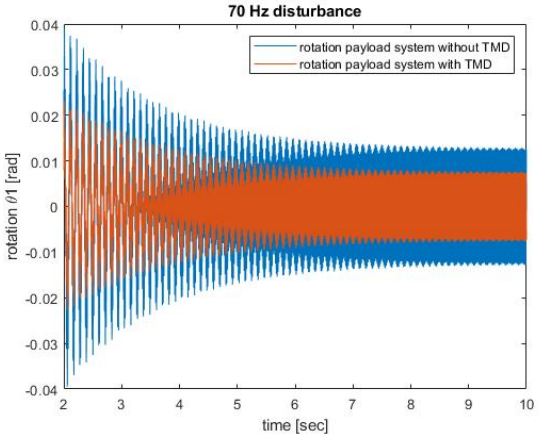

Figure 4.8: Response Payload system with and without TMD at a 70 Hz disturbance.

4.4 SUMMARY

In this chapter the results lead to the following conclusions:
1. Gradient-based optimization based on sole data leads to the same optimal stiffness and damping values as obtained for the passive TMD system.
2. The model for online parameter optimization serves as a basis for measurement results in the next chapter.

CHAPTER 5

MEASUREMENT RESULTS

This chapter will demonstrate the use of a data-based optimization scheme in finding the optimal parameters of an active TMD that maximize energy dissipation. In Section 5.1 the real life setup is discussed with a short list of its key components. Prior to finding the optimal parameters, we need to identify the dissipative elements already present in the structure. The problem that otherwise occurs with such elements will be explained in Section 5.2. In Section 5.3 solutions toward solving this problem are discussed. In Section 5.4, the frequency responses $\frac{\theta_1}{U}$ and $\frac{\theta_2}{U}$ of the real life setup are compared with those obtained from simulations in the earlier chapters. In Section 5.5, it is demonstrated that maximum energy dissipation associates with preferred vibration isolation properties of the payload structure. This chapter is concluded with an outlook in Section 5.6.

5.1 EXPERIMENTAL SETUP

Figure 5.1 depicts the real live setup. Key components are identified by a number. Herein, number 1 en 2 represent the mass inertia, respectively of the payload and the TMD. Number 3,4 and 5,6 represent the actuator and encoder, respectively of the payload and the TMD. Number 7 and 8 represents the transconductance amplifier of the payload respectectively of the TMD. Number 9 represents the data acquisition system and number 10 is the shunt resistor.

5.2 DISSIPATIVE ELEMENTS ALREADY PRESENT IN THE SYSTEM

In this section the influence of dissipative elements already present in the system will be explained. Note that for the simulations in Chapter 3, the initial value of the damping d_2 was chosen at zero. The absence of damping is unlikely to occur in practice, which is the case for the experimental setup where a damping value is found of 5e-5 Nms/rad ; recall Section 2.3.4. This value must be taken into account

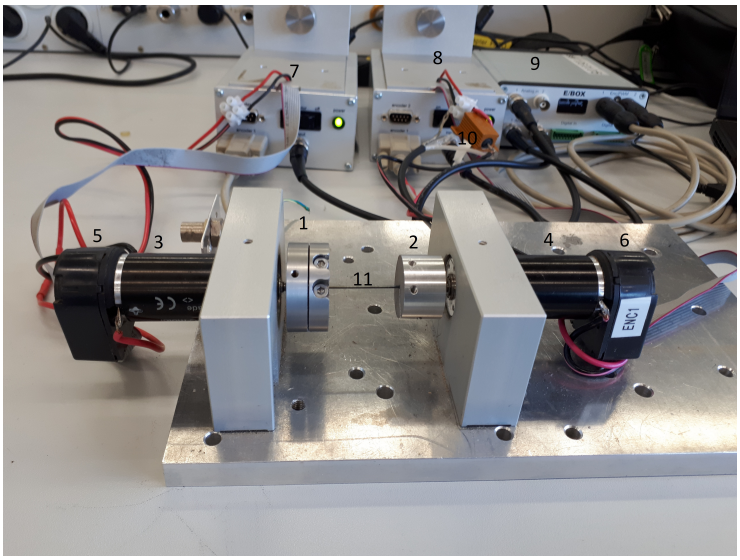

Figure 5.1: Real-life TMD system.

when determining the total energy. Figure 5.2a depicts the simulation of the energy dissipation of the controller and the damper ($D_2 + d_2$), this is the so-called total energy dissipation contrary to the energy dissipation of controller D_2. The maximum energy dissipation of the controller is reached after 5 iterations. The total energy increases continuously until a maximum is reached. The optimal values for the gain Kp_2 and damping D_2 are found while using the total energy criterion, the optimal values are given in Figure 5.2b. The internal energy dissipation in damper d_2, however, cannot be measured in the current experimental setup, where only the energy dissipation derived from the output of the PD controller can be accessed. Figure 5.3a gives the time response of θ_1 and θ_2 while being optimized for the total energy dissipation and Figure 5.3b gives the time response while optimizing on only a part of the total energy dissipation, i.e., the part associated with the PD controller. The latter disregards the energy dissipation in the passive damper d_2. With an optimally tuned TMD, the rotation of θ_1 reached a minimum of 0.012 radians RMS (shown in Figure 5.3a) whereas optimized only on the dissipated energy of the controller, the rotation of θ_1 is equal to 0.018 radial RMS, as shown in Figure 5.3b,which is not optimal for the system as a whole.

5.3 How to estimate total energy dissipation in practice

The total energy dissipation can be determined in two ways. First by identification of the dissipative elements already present in the structure and estimate the sum of

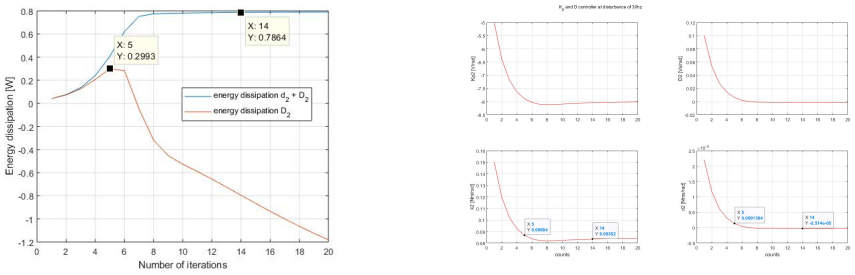

(a) (b)

Figure 5.2: (a) estimated energy dissipation. (b) settings PD controller.

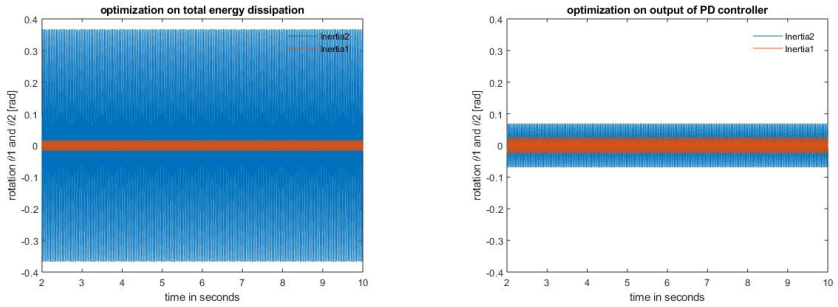

(a) (b)

Figure 5.3: (a) optimized on total energy dissipation. (b) optimized on total energy dissipation.

these dissipative elements with respect to the energy dissipation of the controller. Second, by measuring the energy dissipation by using two data acquisitions systems. The latter is advantageous from the data-based perspective, because it requires no extra prior knowledge of the system. However, this method had not been applied in this report for practical reasons, see appendix C for more discussion.
Figure 5.4 depicts the schematics associated with the estimation of the total energy dissipation having additional disspative elements present in the system. Output to the scheme is the partial and the total energy dissipation.
The partial energy $E_{partial}$ is defined by

$$E_{partial} = mean\left((\dot{\theta}_1 - \dot{\theta}_2)^2 U_2.amp.K_e\right), \tag{5.1}$$

with U_2 the voltage over the shunt resistor, amp is the sensitivity of the shunt resistor and K_e is the torque constant of the actuator.
The Total energy E_{total} is defined by

$$E_{total} = mean\left((\dot{\theta}_1 - \dot{\theta}_2)^2 (U_2.amp.K_e + d_2)\right). \tag{5.2}$$

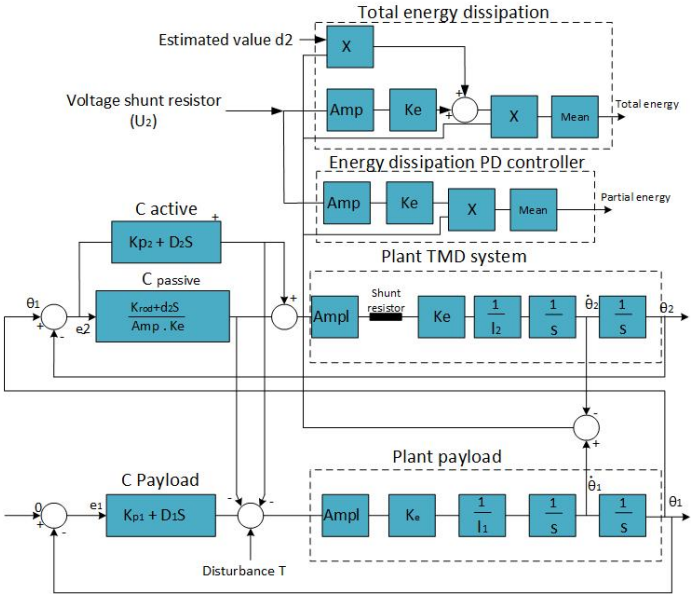

Figure 5.4: Simulation scheme used for determine total energy dissipation.

5.4 VALIDATION OF FRF MEASUREMENTS

In this section, measurement results are presented of the frequency response function θ_1/U and θ_2/U which are compared with the results obtained from numerical simulations, and which serve the purpose of validation of the model of the setup. The frequency response functions are determined with gain Kp_2 of the PD controller at -5 V/rad. A more negative gain is not possible because otherwise the PATO amplifier will saturate. Figure 5.5 depicts the measured frequency response function θ_1/U, which is compared with the model with active controller elements (see Figure 3.13). The frequency response measurements are carried out with white noise as excitation signal with a frequency up to 250 Hz. The resonance (at 42.5 Hz) coincides, but the anti-resonance occurs at lower frequencies than with the parametric model. Figure 5.6 depicts the measured frequency response function θ_2/U in comparison with the active controller elements. Up to 150 Hz the parametric model matches well with the non-parametric model, but at higher frequencies sampling delay as well as a poor signal-to-noise ratio causes deviation between both models.

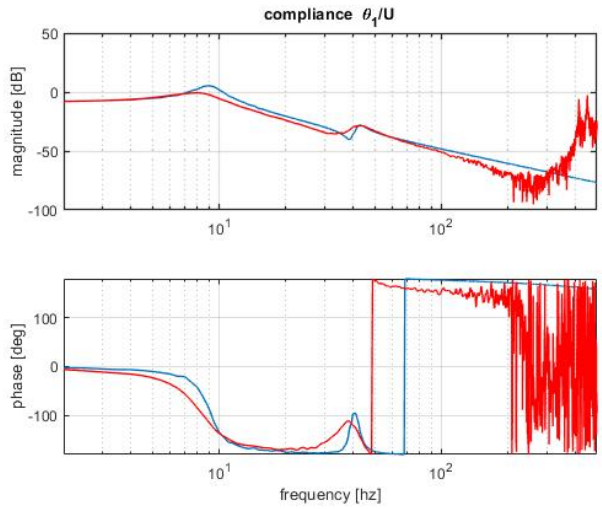

Figure 5.5: Measured frequency response function θ_1 over U.

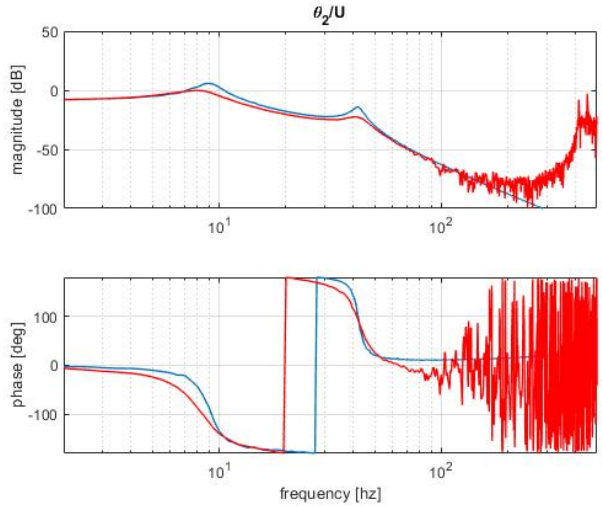

Figure 5.6: Measured frequency response function θ_2 over U.

5.5 MAXIMAL ENERGY DISSIPATION ON REAL-LIFE TMD SYSTEM

In this section, a relation between the total energy dissipation and the rotation of the first mass θ_1 will be examined on the setup. All the simulations in the previous chapters have been done with disturbance frequenies of 5, 30 and 70 Hz, but in the experiments this is not possible because the voltage/current converter saturates. The tested disturbance frequency in the real life setup is therefore chosen at 33 Hz. The experimental results are obtained by means of continuous-time experiments where the mean energy dissipation in all the dissipative elements is determined. Two experiments are done, the first experiment is with a constant gain of Kp_2, which gives the correct anti resonance frequency and by varying the D_2 of the controller. The second experiment is with a constant gain of D_2 (found with the first experiment) and by varying Kp_2 of the controller. Figure 5.7 depicts the energy dissipation and the rotation in radians of the payload system while, varying the damping at a constant gain Kp_2. The maximal energy dissipation is 0.0069 W, and the rotation of θ_1 is 0.0055 radial. The damping coefficient found equals $d_2 = 3.32e^{-5}$ Nms/rad, which is in the same order of magnitude as the dampings coefficient in the simulations at 30 Hz. This experiment confirms the simulation results that maximum energy dissipation leads to optimal vibration isolation performance.

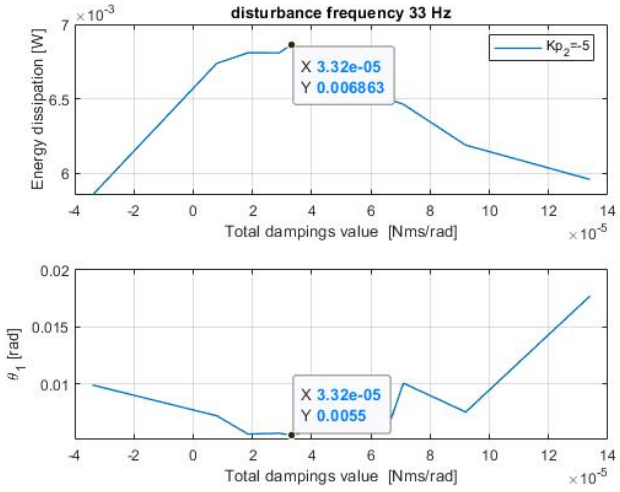

Figure 5.7: Maximal energy dissipation and RMS value of θ_1 while varying D_2.

Figure 5.8 depicts the energy dissipation and the rotation in radians of the payload system while varying the gain Kp_2 with the damping found in the first measurement. The maximal energy dissipation is 0.0069 W, and the rotation of θ_1 is 0.005 rad. The gain of the controller at which maximum dissipation occurs, differs slightly from the gain which gives minimal rotation of the payload. This most likely is caused by

a mismatch in the identification of the damping values of the dissipative elements present in the structure.

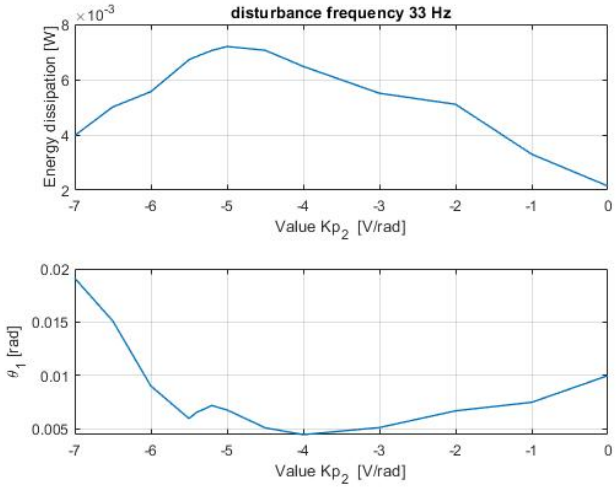

Figure 5.8: Maximal energy dissipation and Rms of θ_1 while varying Kp_2.

5.6 SUMMARY

The results of the simulation are validated on the real setup and the results confirm the conclusions. The experiments demonstrates that maximal energy dissipation implies optimal vibration isolation. Due to practical limitations of the setup it appeared impossible to conduct an automatic data-based optimization such as discussed in Chapter 4. This remains work for future research.

CHAPTER 6

CONCLUSIONS AND RECOMMENDATIONS

This chapter presents the main conclusions of the graduation project and gives recommendations for further research.

6.1 CONCLUSIONS

Maximal energy dissipation will occur at the optimal stiffness and optimal damping values of the TMD. For this maximal energy dissipation level, the influence of the disturbance on the payload is minimized. The simulations demonstrate that maximal energy dissipation implies optimal vibration isolation, not only at a single frequency but at arbitrary harmonic disturbance frequencies. Maximal energy dissipation is found at gradient values of the relevant parameters being equal to zero, hence the possibility to do (online) parameter optimization. It is possible to tune the TMD in real-live to the optimal values of the stiffness and damping coefficient. In online parameter optimization, the energy criterion J does not need an explicit torque measurement but can be estimated through measuring the actuator current, i.e., use the actuator as a sensor. An important finding is that all dissipative elements in the system should be taken into account in the energy dissipation criterion. In this thesis, an estimate is obtained for the damping coefficient of a single (lumped) dissipative element.

6.2 RECOMMENDATIONS

The simulation results differ slightly from the experiments. The cause of these differences should be investigated by estimating the stiffness of the rod and the damping coeeficient more accurately. The applicability of the concept considered in this thesis should be investigated for a broader class of disturbances. Essentially, we envision an adaptively tuned TMD system capable of dealing with any disturbance situation and

constantly driving the vibration isolation system to which it is mounted for optimal isolation performance. In this regard, the use of two ebox is expected to give more accurate results than the currently used method of identification. Such usage is highly recommended for continued research on this topic. Lastly, the machine-in-the-loop approach should be executed in experiment too. For this the current setup is not suited, because of the large transition time in between iterations needed to transfer new models/parameters to (and from) the ebox.

BIBLIOGRAPHY

[1] C. Collette S. Janssens K. Artoos. Active vibration isolation of high precision machines. *DOI 10.1017/S2044820110000134*, August 2010,.

[2] M.A. Beijen. Disturbance feedforward control for vibration isolation systems. *PhD thesis, Eindhoven University of Technology*, 2018.

[3] P.W.J.M. Nuij. Vibration measurements on lighting ballasts. *Technical report, Eindhoven Philips Centre for manufacturing Technology*, 1997.

[4] BruelKjaer. Quality control in production using energy-flow measurements. *Hungarian Seminar and exhibition on noise control*, 1989.

[5] M Brock P Bruel. Measurements of mechanical power used in quality control. *International congres on intensity*, 1990.

[6] E. Mraber M. Guedri M.N. Ichchou M. Soula. A new reliability based optimization of tuned mass damper parameters using energy approach. *Jounal of Vibration and control*, pages 1–18, 2016.

[7] R. Greco G.C. Marano. Optimum design of tuned mass dampers by displacement and energy perspectives. *ScienceDirect*, pages 243–253, June 2013.

[8] M. Abubakar B.J.M. Farid. Generalized den hartog tuned mass damper system for control of vibration in structures. *DOI 10.2495/ERES090171*, pages 185–193, 2009.

[9] S.V. Bakre R.S. Jangid. Optimum parameters of tuned mass damper for damped main system. *Wiley InterScience*, pages 448–470, April 2006.

[10] F. Stroscher. Tuned mass dampers. *Seminar:Vibration and Structure-Borne Sound in Civil Engineering*, March 2006.

[11] I. Nishimura M. Sakamoto N. Koshika S. Ohrui. Active tuned mass damper. *Smart Materials and Structures, Volume 1, Number 4*, August 1992.

[12] maxon product range 2020/21. pages 134–135.

[13] J. den Hartog. Mechanical vibrations . *Book ISBN-10: 0486647854*, 1940.

[14] T. Pinkaew Y. Fujino. Effectiveness of semi-active tuned mass dampers under harmonic excitation. *ScienceDirect Engineering Structures, Volume 23 Issue 7*, pages 850–856, 2001.

[15] M. Zilletti S. J. Elliott and E. Rustighi. Optimisation of dynamic vibration absorbers to minimise kinetic energy and maximise internal power dissipation. *journal of sound and vibration, volume 331, no. 18*, page 4093–4100, 2012.

[16] W. Cui L. Zuo. Dual-functional energy-harvesting and vibration control: electromagnetic resonant shunt series tuned mass dampers. *Journal of vibration and acoustics Volume 135 DOI 10.1115/1.4024095*, pages 051018–1 until 051018–9, October 2013.

[17] F. Weber C. Boston M. Maslanka. An adaptive tuned mass damper based on the emulation of positive and negative stiffness with an mr damper. *Smart Materials and Structures, Volume 20, Number 1*, pages 1–11, December 2010.

[18] D. Tjepkema J van Dijk H.M.J.R. Soemers. Sensor fusion for active vibration isolation in precision equipment. *Journal of Sound and Vibration, Volume 331, Number 4*, pages 735–749, February 2012.

[19] M.F. Heertjes. Data-based motion control of wafer scanners. *IFAC international workshop on adaption and learning in control and signal processing, Volume 49, Issue 13*, pages 1–12, 2016.

[20] M.F Heertjes B Temizer. Data-based control tunning in master-slave systems. *American Control Conference*, pages 2461–2466, June 2012.

[21] H. Hjalmarsson. Iterative feedback tuning an overview. *International journal of adaptive control and signal processing, Volume 16, Issue 5*, pages 373–395, 2002.

[22] S.H. Kamali M. Moallem S. Arzanpour. Self-tuning active tuned mass damper utilizing constrained multi-variable sliding mode extremum-seeking. *Conference on Control Technology and Applications, DOI 10.1109/CCTA.2018.8511338*, 2018.

APPENDIX A

SIMULATION RESULTS OF THE PASSIVE TMD SYSTEM UNDER A 70 HZ DISTURBANCE

Figure A.1 depicts the influence of the disturbance at a frequency of 70 Hz. This frequency is above the resonance frequency of the payload system and the TMD system. In this case the stiffness of the rod should be increased (add positive stiffness) to suppress the disturbance of 70 Hz. Figure A.1 depicts the maximal energy dissipation at a disturbance frequency of 70Hz. Maximum energy dissipation at a given disturbance occurs if k_{rod} = 0,44 Nm/rad and $d_2 = 7,25e{-}5$ Nms/rad.

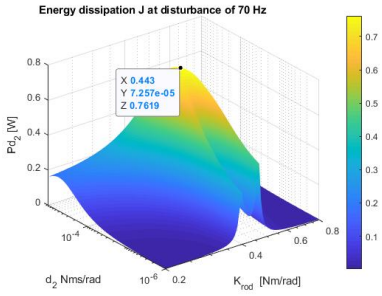

Figure A.1: Maximal energy dissipation at disturbance of 70 Hz.

Figure A.2 shows the influence of the disturbance at the payload system at a disturbance frequency of 70 Hz. With an optimally tuned TMD, the rotation of $\theta_1 = 5,23e^{-3}$ radians whereas with no TMD is applied, the rotation of θ_1 is equal to $9e^{-3}$ radial. The disturbance reduction is again 42%. The stiffness value maximum mean energy dissipation corresponds with the stiffness value when rotation is minimal ,but there is again a slight difference in damping. The estimated stiffness and damping

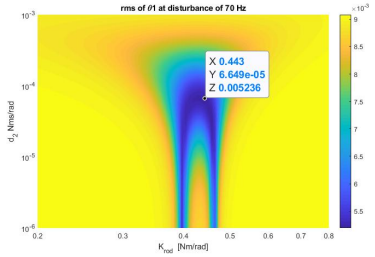

Figure A.2: Rms of θ_1 at disturbance of 70 Hz.

coefficient correpond with the values found with the semi-analytic computations in Section 3.2.

From the above analysis it is concluded that aiming for maximum energy dissipation of the TMD system generally leads to optimal vibration isolation performance of the payload system at arbitrary harmonic disturbance torques.

APPENDIX B

SIMULATION RESULTS OF THE ACTIVE TMD SYSTEM UNDER A 70 HZ DISTURBANCE

In the 3D plots, the gain Kp_2 , D-action D_2 and energy dissipations Pd_2 are displayed. In Figure B.1a, where the disturbance frequency is chosen beyond the resonance frequencies of the payload system and TMD it is shown that the RMS energy dissipation is maximal if the D action D_2 is at its boundary value of 1 $10^{-}6$ Vs/rad and Kp_2 is equal to 9.167 V/rad. The effective stiffness between the two ineria's can be estimated from the passive and active part. The effective stiffness between the two inertias is equal to $K_{rod} + Kp_2 * K_e * ampl$ = 0.4612 Nm/rad

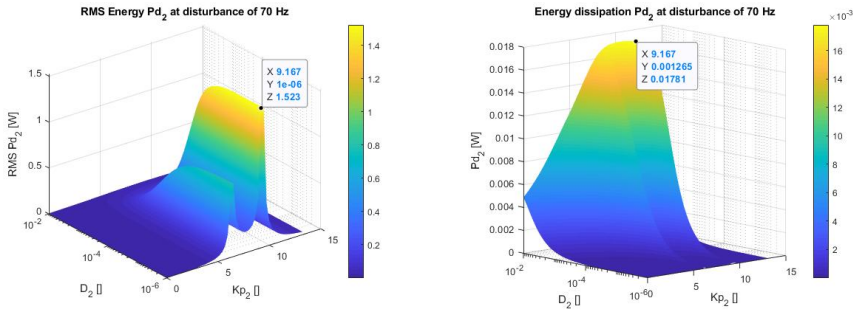

(a) (b)

Figure B.1: (a) rms dissipated energy controller (b) mean dissipated energy controller

This calculated effective stiffness corresponds with an antiresonance frequency of 69.8 Hz estimated with Equation (3.10). Figure B.1b shows approximately the same stiffness at the maximal dissipated energy but, the energy dissipation is much lower than the RMS energy dissipation. The MEAN energy dissipation is maximal at a

damping constant D_2 of 1.265 10^{-3} Vs/rad.

The effective damping between the two ineria's is given by:

$$\begin{aligned} D^{eff} &= D_2 * K_e * ampl \\ &= 2.77\ 10^{-5} Nms/rad \end{aligned} \tag{B.1}$$

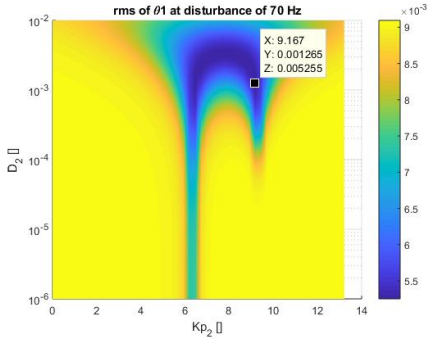

Figure B.2: rms rotation θ_1 at disturbance of 70 Hz

Figure B.2 depicts the influence of the disturbance at the payload system. In this 3D plot, the gain of the controller Kp_2, D action D_2 and rms value of θ_1 are displayed. With an optimally tuned PD controller, the rotation θ_1 has a minimum of $5.2e^{-3}$ radians and with no TMD applied, the rotation of θ_1 is equal to 9^{-3} radial. The improvement of vibration isolation properties of the payload system in terms of disturbance reduction is therefore 42%. This optimal value for the rotation of θ_1 occurs at the optimal PD controller values regarding maximal energy dissipation shown in Figure A.1. As such, it is concluded that also in the active case aiming for maximum energy dissipation translates well to the objective of optimal vibration isolation performance in view of a harmonic disturbance torque at 30 Hz.

APPENDIX C

DETERMINE ENERGY DISSIPATION USING TWO DATA ACQUISITION SYSTEMS

Figure C.1 depicts the simulation schematics associated with use for two data acquisition systems for determining the total energy dissipation. Output to the scheme is the total energy dissipation. The total energy dissipation is estimated indirectly by measuring the voltage over the shunt resistor. The torque determined with the current is obtained by multiplying the voltage over the shunt with the sensitivity of the shuntresistor Amp and with the torque constant of the actuator K_e. The total energy dissipation is estimated through the product of the torque and the velocity difference of $\theta_1 - \theta_2$, see figure C.1.

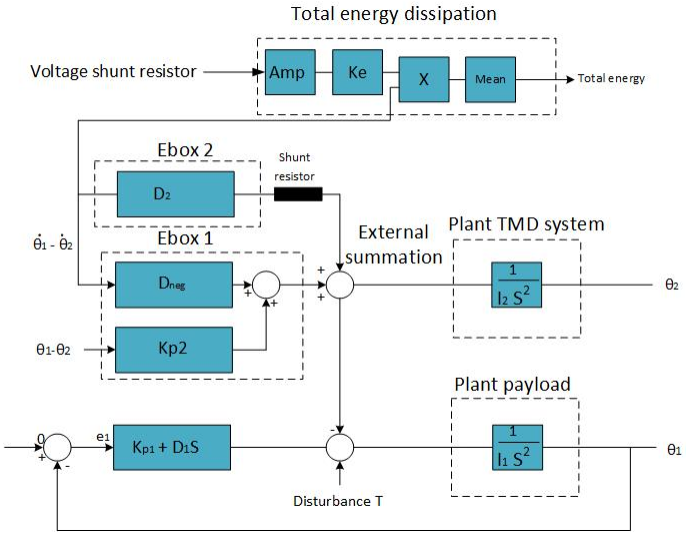

Figure C.1: Simulation scheme used for estimate total energy dissipation.